sustainability

MDPI

Article

Innovative Design Concept of Cooling Water Tanks/Basins in Geothermal Power Plants Using Ultra-High-Performance Fiber-Reinforced Concrete with Enhanced Durability

Salam Al Obaidi [1,2,*], Patrick Bamonte [1], Francesco Animato [3], Francesco Lo Monte [1], Iacopo Mazzantini [3], Massimo Luchini [3], Sandra Scalari [3] and Liberato Ferrara [1]

[1] Department of Civil and Environmental Engineering, Politecnico di Milano, 20133 Milan, Italy; patrick.bamonte@polimi.it (P.B.); francesco.lo@polimi.it (F.L.M.); liberato.ferrara@polimi.it (L.F.)
[2] Roads and Transportations Engineering Department, University of Al-Qadisiyah, Diwaniyah 58001, Iraq
[3] Enel Green Power, 00198 Rome, Italy; francesco.animato@enel.com (F.A.); iacopo.mazzantini@enel.com (I.M.); massimo.luchini@enel.com (M.L.); sandra.scalari@enel.com (S.S.)
* Correspondence: salammaytham.alobaidi@polimi.it

Abstract: The structure presented in this paper is intended to be used as a prototype reservoir for collecting water coming from the cooling tower of a geothermal plant, and is primarily designed to compare the performance of different materials (traditional reinforced concrete and Ultra-High-Performance Fiber-Reinforced Concrete (UHPFRC)) as well to assess the performance of different structural solutions (wall with constant thickness versus wall provided with stiffening buttresses). In the absence of specific code provisions, given the novelty of the UHPFRC used, the main properties used for the design were determined through a dedicated experimental campaign (tensile/flexural properties and shrinkage). The main focus of the design was on the Serviceability Limit States, more specifically the requirements regarding water tightness. Given the rather simple structural layout, especially in the compartments where no stiffening buttresses are present, linear elastic analysis was used to determine the internal actions. The nonlinear behavior ensuing from the peculiar tensile constitutive response of the material was taken into account locally, in order to determine the stress level, the depth of the compression zone and the crack width. The performance was finally compared with the reference compartment (made with ordinary reinforced concrete), through on-site observations and measurements.

Keywords: durability; UHPFRC; water-retaining structures; aggressive environment

Citation: Al Obaidi, S.; Bamonte, P.; Animato, F.; Lo Monte, F.; Mazzantini, I.; Luchini, M.; Scalari, S.; Ferrara, L. Innovative Design Concept of Cooling Water Tanks/Basins in Geothermal Power Plants Using Ultra-High-Performance Fiber-Reinforced Concrete with Enhanced Durability. *Sustainability* **2021**, *13*, 9826. https://doi.org/10.3390/su13179826

Academic Editors: Fausto Minelli, Enzo Martinelli and Luca Facconi

Received: 7 July 2021
Accepted: 29 August 2021
Published: 1 September 2021

1. Introduction

Reinforced concrete structures under Extremely Aggressive Exposure (EAE) are known to suffer from durability and time-dependent problems, which require continuous repair actions that are critical regarding the economic impact and service disruption problems (especially in the case of strategic infrastructures, including harbors, highways or facilities for the production of energy) [1]. Typical pathologies in reinforced concrete structures under EAE conditions consist of excessive corrosion of the steel reinforcement, accompanied by cracking and spalling of the concrete cover. Corrosion is typically initiated by altering the pH environment of the concrete, particularly in the vicinity of the steel reinforcement (concrete cover) or by localized chloride attack to the reinforcement. This mechanism may occur, e.g., in concrete structures that are in contact with extremely aggressive waters (industrial chemical water, marine or deicing salts environments). Following the prescriptions to design a structure with a specific service life under extremely aggressive exposure conditions, designers are obligated to focus on the quality of the concrete cover to ensure its ability to protect the reinforcement from corrosion, at least prior

to reaching the design target service life. Furthermore, reinforced concrete structures in industrial applications are also severely prone to corrosion and erosion due to the harsh environment created by the chemical treatment and processing methods. Among the aggressive exposure conditions, the XA3 exposure class (highly aggressive chemical environment) has been reported in many industrial and chemical applications as well as in one of the case studies selected as the topic of the present paper: the basins for a cooling tower in geothermal power plants owned and run by Enel Green Power in different sites in Tuscany (Italy), which have suffered from cracking, loss of waterproofing layers, as well as abrasion and erosion of the concrete due to the exposure to the geothermal water, actually containing different types of aggressive chemicals, including chloride and sulfate ions [2]. Since these degradation mechanisms required quick maintenance works in order to maintain the plants in operation, repairing of the degraded concrete layers, sealing of the joints between the bed and walls, adding non corroded construction elements and reapplying the bituminous coating have been conducted at the deteriorated parts of the artefacts to extend their service life. However, some parts could not be retrofitted due to limited maintenance time.

Currently available design codes and related standards specify, depending on the exposure class and required service life, the structural design criteria, such as the crack-width limits, as well as detail the criteria, including minimum cover thickness, and material criteria, including type of cement and w/c content, to meet the durability requirements specifically limiting the ingress of chemical aggressive and to provide a design service life of 50 to 100 years. As a matter of fact, the aforementioned deterioration scenarios may also appear in the early stages of the structure's operational life, likely due to the inherent characteristics of ordinary reinforced concrete materials and/or lack of experience during the construction. Therefore, the use of advanced alternative materials and of the corresponding construction and design methodologies need to be implemented in the design and construction of structures and infrastructures, with specific focus on extremely aggressive environments.

Currently, in both industry and academia, there is significant driving momentum in the development and application of advanced cement-based materials in the construction and retrofitting of structures and infrastructures, to provide them with enhanced durability and hence extended service life and overall improved environmental and economic sustainability. In this respect, Ultra-High-Performance Concrete (UHPC) or Ultra-High-Performance Fiber-Reinforced Concrete (UHPFRC), with its highly compact matrix and ability to control and distribute the induced damage into multiple and narrow cracks, representing its most resilient features, is the material to be implemented for applications demanding superior durability in real structural service conditions, which, for cement-based material, is necessary to be considered in the cracked state [3,4].

In addition, the peculiar composition of UHPFRCs, featured by a high content of cement and of supplementary cementitious materials with a low water/binder ratio, is highly conducive to autogenous healing of the cracks [5–7], which can be furthermore stimulated through the addition of crystalline mineral additions, mineral admixtures and other tailored constituents, including SAPs [7–10]. The improvement of mechanical performance achieved through the synergy of the mix composition and the presence of steel fibers in further interaction with the aforementioned enhanced durability and self-healing features may make the development and application of UHPFRCs able to improve the environmental footprint, thanks to optimized use of material, and significantly extend the structure service life in extremely aggressive environments [11–13]. Moreover, thanks to their recently demonstrated high recyclability potential, this category of material is also able to bring a breakthrough innovation into the concept of longer structural service life [14].

As a matter of fact, current solutions for new concrete constructions in EAE have so far seldomly implemented on a massive scale advanced cement-based construction materials, such as Ultra-High-Performance (Fiber-Reinforced) Concrete (UHPC/UHPFRC),

mainly because of a lack of standards and of technical awareness by most designers and contractors. Having said that, to date, the claimed superior durability of UHPC/UHPFRC has been almost exclusively demonstrated by means of laboratory specimens, focusing mainly on the uncracked state. To contribute in filling this gap between laboratory testing and real-scale structural applications, the EC H2020-funded ReSHEAience project aims to test and validate new design concepts through long-term monitoring of six proof-of-concept pilot structures, selected as representative of the cutting-edge economy sectors such as green energy, blue growth and conservation of reinforced concrete heritage [15]. The focus of this work is on the pilot constructed within the framework of ReSHEALience project and located in Enel Green Power geothermal power plant in the municipality of Chiusdino in Tuscany (Italy), namely, a geothermal cooling tower water collection basin. The basin is operating in parallel with the actual basins of the plant. The main pathologies in the basins containing the geothermal water are cracking produced by expansion (sulphate attack), cement paste dissolution (leaching) and/or efflorescence (acid attack), together with reinforcement corrosion triggered by the chlorides also present in the water. In the project framework outlined above, the geothermal basin of the Chiusdino plant has been redesigned to resist the mechanical actions and chemical attack as well. With the aim of implementing a signature durability-based design of concrete structures, which through the incorporation of degradation mechanisms into structural design algorithms [16] will contribute to move from a prescriptive to performance-based design approach [17–21], three types of structural concrete solutions have been designed and constructed. They consist of the following:

(a) A 100 mm-thick cast-in-place ordinary reinforced concrete wall.
(b) A 60 mm-thick cast-in-place UHPC wall.
(c) A solution consisting of 30 mm-thin precast UHPC slabs "supported" by 200 × 200 mm^2 cast-in-place UHPC columns/buttresses.

The aim of this paper is to analyze each structural solution both at the serviceability and ultimate limit states, based on the mechanical properties of the materials experimentally identified through a tailored experimental campaign [22]. Moreover, dedicated tests are also being conducted on the basin to validate the proof of concept behind each structural system, as also affected by the different construction methods implemented on the construction site. The general aim of the work is to pave the way toward a performance-based design approach for long-term durability of UHPFRC structures, also in the context of the currently ongoing international code-writing and standardization efforts.

2. Description of the Pilot

Within the framework of the ReSHEALience project, the main aim is to upgrade the concept of UHPC/UHPFRC to Ultra-High-Durability Concrete (UHDC) by implementing macro- and nanoscale constituents in strain-hardening steel fiber-reinforced cementitious material [15]. The purpose of this "tailoring" the UHDC material concept is to enhance the durability in real structural service scenarios, which explicitly include the presence of "micro-cracks", as further explained, as a natural "status" of the material into its service state, thus reducing the need and frequency for maintenance and the related costs, and contribute to wholesome extension of the service life of structures subjected to extremely aggressive environments. The most distinguished characteristics of the UHDC materials employed in this project is the incorporation into the mix-design of selected nano-constituents, namely, alumina nano-fibers and cellulose nano-crystals, which, besides contributing to enrich the microstructure of the concrete matrix and preventing or reducing the transport of aggressive substances in the uncracked state [23–25], also provide functionalities such as self-curing [20,21] and, in main synergy with crystalline admixtures, stimulate autogenous healing [26]. Moreover, as reported in the literature [27–30] and proven by [23], the signature mechanical tensile behavior of UHPFRC is characterized by a stable multiple cracking process, which spreads the localized damage into multiple tiny cracks

up to a relatively higher deformation level as compared not only to plain and reinforced concrete but even to ordinary fiber-reinforced concrete (FRC). This unique feature may allow and require tailored structural concepts to be designed for its full exploitation, not merely confined to the reduction of structural element thickness. This step is fundamental in order to tackle the challenges brought in by the newly developed materials and to formulate a holistic durability-based structural design approach, which will be validated through the innovative structure concepts designed, built and tested, of which the tank to collect and contain the geothermal water dealt with in this paper is a landmark representation in the framework of the project [31].

The structure consists of a 300 mm-thick foundation slab made of ordinary reinforced concrete, and is divided into three compartment basins by means of vertical partitional walls. The in-plan dimensions of the whole tank are approximately 22.50 × 7.00 m^2. The three basins are characterized by the same in-plan dimensions (7.50 × 7.00 m^2), but differ in materials and structural typology: one in ordinary reinforced concrete (RC) and the other two in Ultra-High-Durability Concrete (UHDC). The vertical walls, which characterize the three compartments, have different thicknesses, depending on the material used and the geometry of the structural elements (Figure 1).

Basins 1 and 2 consist of cast-in-place continuous walls with a constant thickness, respectively, equal to 100 mm for the ordinary reinforced concrete Basin 1 and 60 mm for the UHDC Basin 2. Basin 3, on the other hand, consists of 30 mm-thick precast slabs, stiffened by cast-in-place vertical buttresses with a square cross section (200 × 200 mm^2) also made of UHDC, and spaced at a mutual distance of 1.50 m on the long side and 1.40 m on the short side. The dimensions chosen for the buttresses are in line with those needed in similar structures to ensure adequate support for the wooden superstructure.

When the picture in Figure 2a was taken (20 February 2020), the structure was almost completed, with only some of the columns of Basin 3 still to be cast. Figure 2b shows the structure completed and filled with geothermal water during one of the validation tests, performed on 20 April 2021.

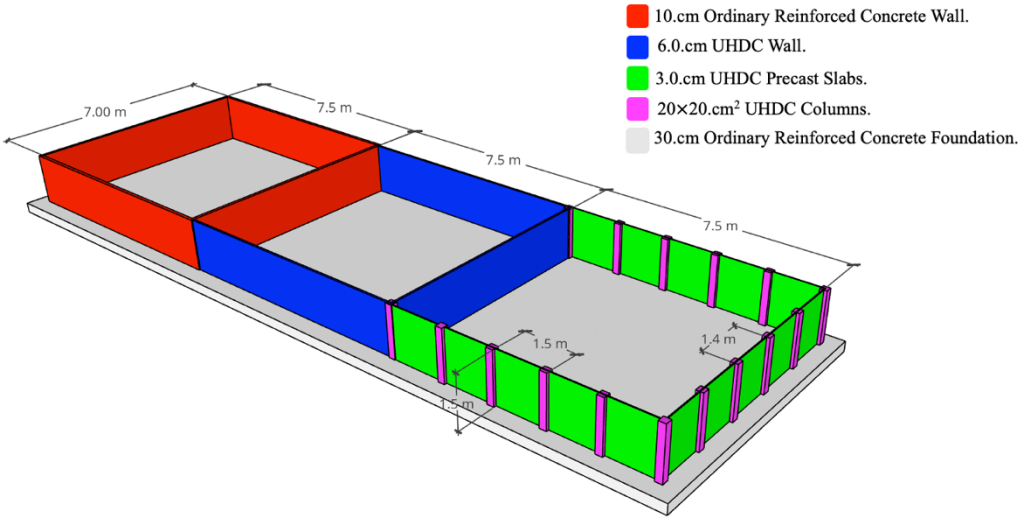

Figure 1. Geometrical and material description of the basins.

Figure 2. Pictures of the structure, taken on 13 February 2020 (**a**) and on 20 April 2021 when a full load test was performed filling the three basins (**b**).

3. Materials

3.1. Reinforced Concrete (Basin 1)

For the foundation slab and the four walls made with the ordinary reinforced concrete traditional solution, concrete C25/30 was used, characterized by the following mechanical properties (EN 1992-1-1[32]):

- Characteristic cylindrical compressive strength: f_{ck} = 25 MPa.
- Average direct tensile strength: f_{ctm}= 2.6 MPa.
- Average indirect tensile strength (in bending): f_{cfm} = 3.1 MPa.
- Instantaneous modulus of elasticity: E_{cm} = 31 GPa.

The values of the average direct and indirect tensile strength as well as of the Young's modulus of elasticity correspond to the concrete class chosen, as indicated in the Italian Standard (NTC 2018 [33]), and are in line with those reported in EN 1992-1-1 Table 3.1

[32]. Nonetheless, a Schmidt hammer (rebound hammer) tester was used to evaluate the concrete compressive stress of the reinforced concrete walls and the foundation. The results indicated average values of 28–37 MPa, as converted to characteristic cylindrical values.

3.2. UHDC (Basins 2 and 3)

The UHDC mix used for the other two compartments, whose mix design and chemical compositions of the employed cement and slag are shown in Tables 1 and 2, respectively, is characterized by the presence of dispersed fiber reinforcement, to the advantage of the overall mechanical behavior, which allowed structural solutions without the need of a specific traditional reinforcement. The straight brass-plated fibers, with the characteristic length and diameters being 20 mm and 0.22 mm, respectively, provide the minimum tensile strength of 2400 MPa. In consideration of the peculiarities of the material, a specific experimental campaign of mechanical characterization was performed in order to investigate the post-cracking behavior, especially focusing on the multi-cracking stage [34].

All the mechanical tests were performed after at least 90 days after casting, in order to limit the possible influence brought in by the delayed hydration of the slag. In the curing period, all specimens were stored in controlled environmental conditions (RH = 90%, T = 20 °C).

Different testing methods have been carried out in order to investigate the multiple cracking phenomena experienced by the UHDC under tensile and flexural loads, as shown in Figure 3. Indirect tensile tests have been performed employing the so-called Double Edge Wedge Splitting (DEWS) test methodology, able to provide in a straightforward manner the tensile stress–COD (Crack Opening Displacement) relationship of the material. Moreover, flexural 4-Point Bending Tests (4PBT) were also performed on the deep and thin beams, as below:

- Deep beams—DB ($L \times b \times h = 500 \times 100 \times 100$ mm^3);
- Thin beams—TB ($L \times b \times h = 500 \times 100 \times 25$ mm^3).

The 4PBT on thin beams were adapted to verify the effects of fiber orientation in a "structural" specimen with the same thickness employed in the construction of the basin walls.

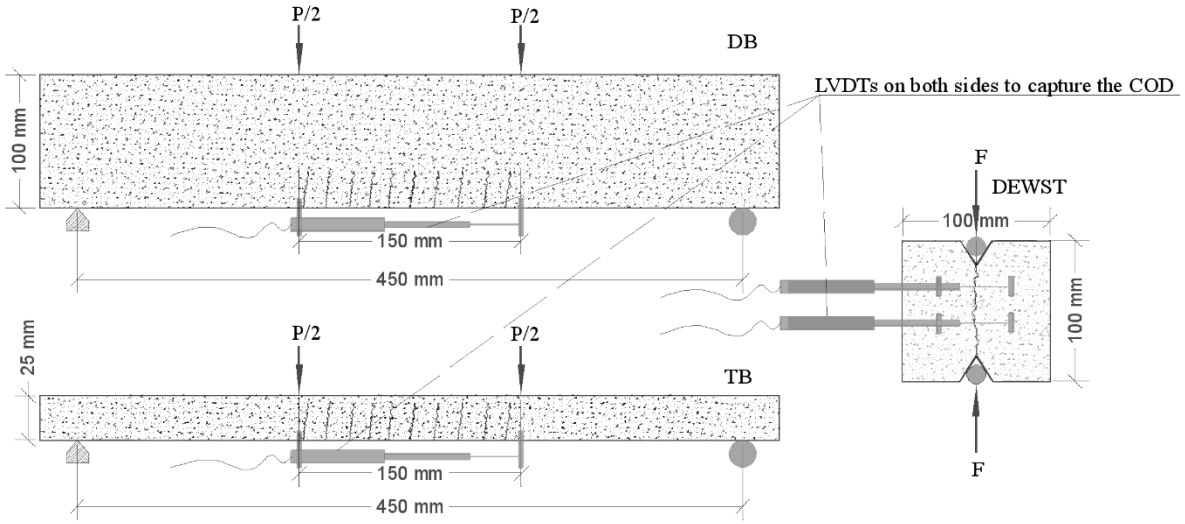

Figure 3. Different types of mechanical tests to evaluate the tensile behavior of UHDC: 4PBT under flexural load P, for the deep beam (DB) and thin beam (TB), and an indirect tensile test, Double Edge Wedge Splitting (DEWST), under load F.

In Figure 4, the experimental nominal flexural stress σ_n (black curves) is plotted as a function of the Crack Opening Displacement (COD) for the reference mix, as measured

across a 150 mm-wide central zone from the 4-Point Bending Tests on deep (Figure 4a) and thin beams (Figure 4b). The nominal stress is evaluated as follows:

$$\sigma_n = \frac{PL/6}{bh^2/6} = \frac{PL}{bh^2} \quad (1)$$

where P is the total load applied (N), L is the distance between the two supports (450 mm for both DB and TB), and b and h are the specimen width and height in mm, respectively. In the same plots, the response simulated employing the tensile stress–COD constitutive response calibrated on the basis of the DEWS tests [35] is shown (pink curves). In addition, for design purposes, the red curves show the results obtained assuming an elastic–perfectly plastic constitutive law, with the direct tensile strength equal to 7.0 MPa; up to a COD approximately equal to 2.0 mm, the numerical results are in good agreement with the experimental results as described in details in [22], where all the mechanical parameters below were calibrated.

As a consequence, the following mechanical properties were assumed (including a dispersion coefficient γ_d = 1.25 as per prescriptions contained in *fib* Model Code 2010):

- Average direct tensile strength: f_{ctm} = 7.0/1.25 = 5.6 MPa.
- Average indirect tensile strength (in bending): f_{cfm} = 12.0/1.25 = 9.6 MPa.
- Instantaneous modulus of elasticity: E_{cm} = 41.7 GPa.

Table 1. The Ultra-High-Durability Concrete (UHDC) mix components and their proportions.

Constituents	XA-CA	XA-CA + ANF	XA-CA-CNC
CEM I 52,5 R (kg/m³)	600	600	600
Slag (kg/m³)	500	500	500
Water (liter/m³)	200	200	200
Steel fibers Azichem Readymesh 200® (kg/m³)	120	120	120
Sand 0–2 mm (kg/m³)	982	982	982
Superplasticizer Glenium ACE 300 ® (liter/m³)	33	33	33
Crystalline Admixture Penetron Admix ® (kg/m³)	4.8	4.8	4.8
Alumina nanofibers NAFEN®* (kg/m³)	-	0.25	-
Cellulose nanofibrils Navitas®* (kg/m³)	-	-	0.15

* % by weight of cement.

Table 2. Chemical composition of the employed cement and slag.(LOI: loss on ignition @1000 °C).

Oxide (wt.%)	CaO	SiO_2	Al_2O_3	MgO	SO_3	Fe_2O_3	TiO_2	Mn_2O_3	K_2O	Na_2O	Other	LOI
PC	59.7	19.5	4.9	3.3	3.4	3.5	0.2	0.1	0.8	0.2	0.4	2.5
BFS	39.2	38.9	10.2	6.4	1.3	0.4	0.6	0.3	0.5	0.8	0.3	1.2

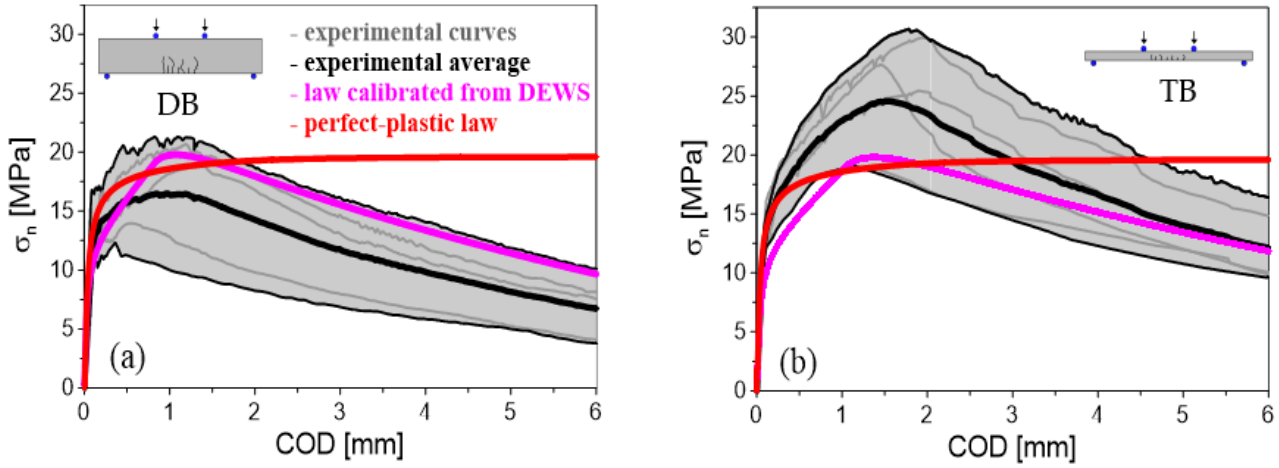

Figure 4. Maximum nominal stress in bending as a function of the Crack Opening Displacement for (**a**) deep beams (DB) and (**b**) thin beams (TB).

4. Structural Analysis

The design of the walls that make up the structure was carried out with reference to the maximum water height (1.50 m), using simple design equations based on a cantilever structural scheme for Basins 1 and 2, and on a slab clamped along three edges for Basin 3 (Figure 5), where the fixity of three edges is guaranteed by the monolithic connection with the buttresses along the two vertical edges and with the foundation slab along the bottom edge, as illustrated in Figure 2.

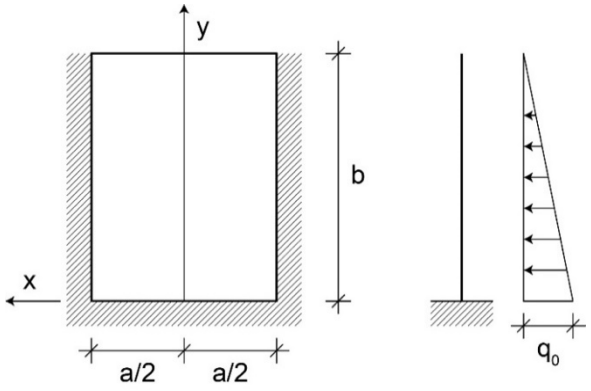

Figure 5. Structural scheme assumed for the design of Basins 1, 2 and 3.

The loads acting on the structure are the self-weight of the structural members, since no particular finishes are foreseen, and the hydrostatic pressure is due to the water contained inside the tank.

The self-weight is calculated on the basis of the specific weight of the materials and the dimensions of the structural elements. The specific weight values assumed are the following:

- Ordinary reinforced concrete: γ_{RC}= 25 kN/m^3.
- Fiber-reinforced cementitious composite: γ_{UHDC} = 25 kN/m^3.

The hydrostatic pressure of the water, acting on the vertical walls and on the bottom of the tank, was calculated by assuming a value equal to γ_w = 10 kN/m^3 for the specific weight of the water.

Two different load conditions were considered, for the serviceability (SLS) and ultimate (ULS) conditions, respectively. In the SLS, the height of the water table, as per the design provisions, is assumed at 1.30 m; at the ULS, an overflow of the water is assumed,

and the maximum water height (h_w) compatible with the bearing capacity of the three basins is determined.

A summary of the design process is shown in Table 3, where a and b are the dimensions of the wall considered (see Figure 5; where $a/b > 1.5$, a one-way cantilever layout was assumed, indicated with symbol ∞ in Table 2), f_{cfm} is the indirect flexural tensile strength, $M_{max.}$ is the maximum bending moment along the y-axis, and $t_{min.}$ is the minimum wall thickness required to keep the maximum normal stress below the indirect flexural tensile strength.

Table 3. Design of the wall thickness of the three basins.

Basin	1 (RC)	2 (UHDC)	3 (UHDC)
a (m)	∞	∞	1.50
b (m)	1.50	1.50	1.50
a/b	∞	∞	1.00
f_{cfm} (MPa)	3.10	9.60	9.60
M_{max} (kNm/m)	5.63	5.63	1.01
t_{min} (mm)	104	59	25

A more refined evaluation of the stresses of the structural members of the tank, including the expected stress concentrations at the corners, was then carried out by means of a three-dimensional finite elements linear elastic model developed with the commercial software MIDAS Gen 2012. The FE model consists of 300 mm-thick horizontal plate elements for the foundation slab and vertical plate elements of different thickness to represent the external and internal walls. The buttresses in the third basin have been modelled using beam elements with a square section (200 × 200 mm^2). A three-dimensional view of the model is shown in Figure 6, where the geometric properties of the plate and beam elements are highlighted with different colors. One of the slabs on each side of Basin 3 has been modelled as 20 mm thick in order to assess the limits of employment of the developed UHDC material.

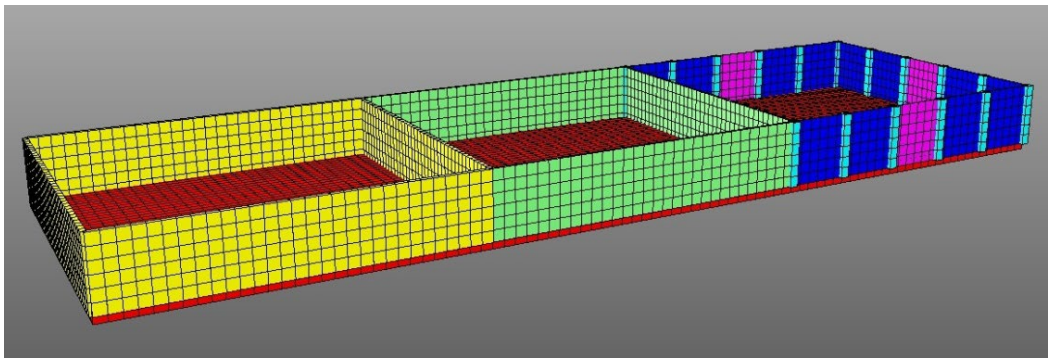

Figure 6. Three-dimensional view of the model used for finite element analysis and geometry of the plate elements (thicknesses: red = 300 mm; yellow = 100 mm; green = 60 mm; blue = 30 mm; magenta = 20 mm) and beams (light blue: section 200 × 200 mm^2).

The interaction between the foundation slab and the soil was accounted for through the Winkler model, with a constant that represents the link (supposedly linear elastic) between the pressure and the corresponding displacement. For the characteristics of the soil, reference was made to a detailed description relating to a similar structure located in the same plant. The characteristics of the soil referred to in the aforementioned report were assumed, due to the proximity between the two sites. In particular, for the purpose of modelling the contact between the foundation bed and the ground, a value of the subgrade stiffness equal to 30 MN/m^3 was assumed

The mechanical and physical properties of the materials for the purposes of structural analysis, i.e., elastic modulus and specific weight, were introduced by defining two materials through the appropriate functions of the code. The analysis linear elastic, tensile and compressive strengths, as well as the reinforcement present in the reinforced concrete elements, did not affect the results.

Given the simple structural scheme that characterizes Basins 1 and 2 (i.e., cantilever wall), attention is focused only on the most significant results obtained for Basin 3, where walls of different thicknesses (20 and 30 mm) were adopted, as explained above. As expected, given the values shown in Table 2, in the 30 mm-thick walls the values of the maximum tensile stress are lower than the value of the indirect tensile strength during bending, f_{ctf} = 9.60 MPa (Figure 7a); on the contrary, the value of f_{cfm} (9.60 MPa) is exceeded in the walls with a thickness equal to 20 mm (Figure 7b).

The fact that that the tensile strength in bending is exceeded in limited portions of the structure should, however, pose no problems, considering that (a) the structure possesses sufficient redundancy to compensate for the limited (and localized) cracking phenomena; and (b) one of the primary objectives of the structure is to provide information about the behavior of UHDC in the cracked state.

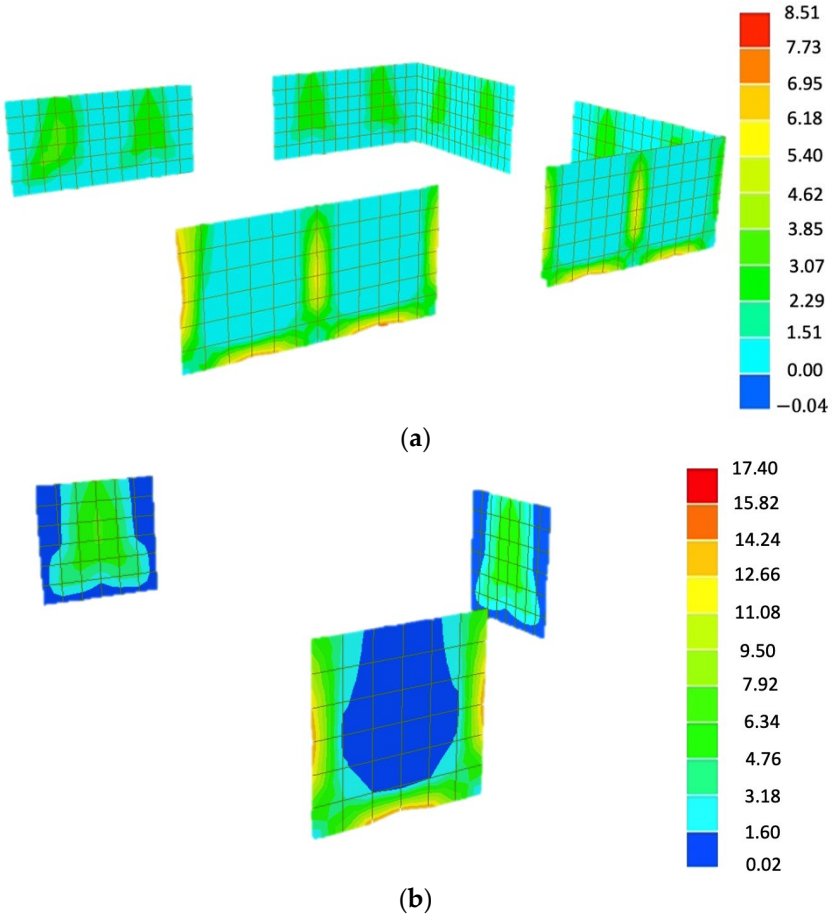

Figure 7. Basin 3: (**a**) maximum tensile stress on the walls with a thickness = 30 mm; (**b**) maximum tensile stress on the walls with a thickness = 20 mm *all units are in MPa.*

4.1. Analysis in Service Conditions (SLS)

The analysis at the Serviceability Limit States of the basins built with UHDC (second and third basin) and ORC (the first basin) was carried out by means of a sectional approach, where the capability of the UHDC material to redistribute the stresses thanks to the contribution of the fibers is explicitly accounted for (Figure 8). For the first basin, the section is not cracked under the service level of water. To this end, compatibility is ensured by assuming that plane sections remain plane, the compression stress distribution is assumed to be linear, while the tensile stresses are assumed to have an elastic–perfectly plastic distribution. As previously mentioned, the maximum tensile stress is limited to the value worked out by Lo Monte and Ferrara [34], namely, 5.60 MPa (coefficient of dispersion included). By enforcing equilibrium, under the maximum bending moment expected in the SLS (M_{SLS}), the strain distribution along the thickness can be determined, and more specifically the maximum tensile strain $\varepsilon_{t,max}$. The expected maximum crack width w_{max} is then worked out by assuming the characteristic length equal to the wall thickness t; therefore, $w_{max} = \varepsilon_{t,max} \times t$.

Table 4 summarizes the results of the SLS design, in terms of tensile and compressive stresses and expected crack widths. Notably, even in the presence of cracking, the estimated crack widths are either very small (Basins 2 and 3b) or nil (Basin 3a), thereby indicating reduced leakage likelihood. In addition, the maximum stress in compression is very low, considering that the UHDC developed attains values of compressive strength that can easily exceed 100 MPa. Thanks to the stress redistribution brought by the behavior of the plate theory [36], sections 3a and 3b show a very low values in terms of acting moments compared the other sections where the cantilever one-way behaviors were dominated.

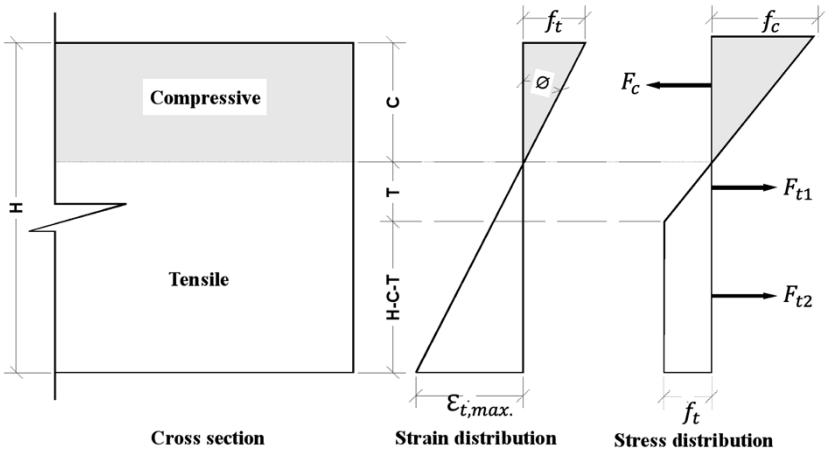

Figure 8. Stress and strain distribution across the thickness of the UHDC section.

Table 4. Evaluation of the state of stress and strain in the r/c and UHDC basins at SLS.

Basin	1	2	3a	3b
h (mm)	100	60	30	20
M_{SLS} (kNm/m)	3.67	3.67	0.67	0.67
$\sigma_{c,max}$ (MPa)	2.17	6.13	4.45	12.86
$\varepsilon_{t,max}$ (‰)	0.006	0.14	0.10	0.39
w_{max} (μm)	-	8	-	8

4.2. Analysis in Ultimate Conditions (ULS)

As previously mentioned, the ultimate limit state condition is evaluated in terms of the maximum height of the water (h_w), assuming overflow to take place, on the basis of the bending capacity *Mu* of the walls. To this end, a yield line analysis was carried out for

the walls assuming a simple cantilever mechanism (global collapse) and a more complex (local collapse) mechanism for the walls provided with buttresses (Figure 9). Clearly, the safety of the walls is sufficient if the maximum height of the water h_w is larger than the height of the wall (b = 1.50 m), since overflows are unlikely to occur.

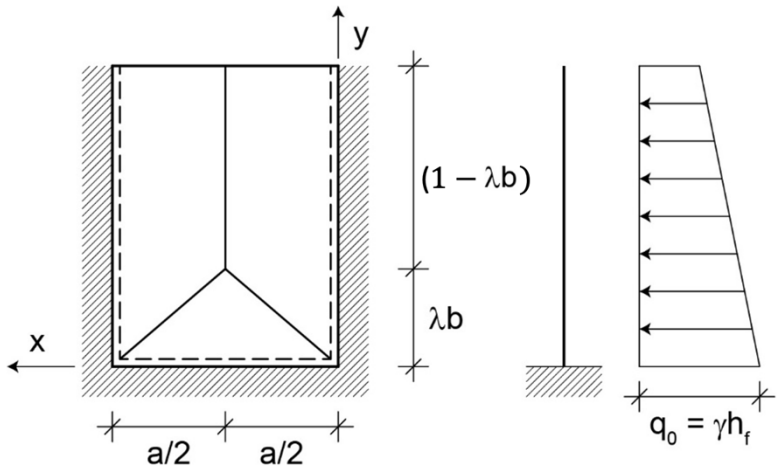

Figure 9. Local collapse mechanism assumed for Basin 3.

The maximum height of the water corresponding to the collapse mechanism shown in Figure 9 can be determined analytically by minimization of the following expression (as a function of the unknown parameter λ):

$$h_w = \frac{\frac{12M_u}{\gamma ab}\left(\frac{a}{b}\cdot\frac{1}{\lambda}+\frac{2b}{a}+\frac{4b}{a}\lambda\right)+\frac{3}{2}b+\frac{\lambda^2 b}{4}}{3-\lambda} \quad (2)$$

where M_u is the ultimate resisting moment in the assumed yield line mechanism section.

The results of the yield line analysis are summarized in Table 5. It is worth noting that for the 100 mm-thick reinforced concrete wall as well as for the UHDC walls with a thickness equal to both 60 and 30 mm, the governing collapse mechanism (i.e., characterized by the lower value of h_w) is the global mechanism, while for the assumed lowest value of the thickness the minimum value is obtained for the local mechanism. In all cases, however, $h_w > h$ (Figure 10).

Table 5. Evaluation of the maximum water height, h_w , in the UHDC basins at ULS.

Basin	**1**	**2**	**3a**	**3b**
t (mm]	100	60	30	20
M_u (kNm/m)	14.0	10.08	2.52	1.12
Mechanism	Global	Global	Global	Local
h_w (m)	2.63	1.90	2.55	2.28

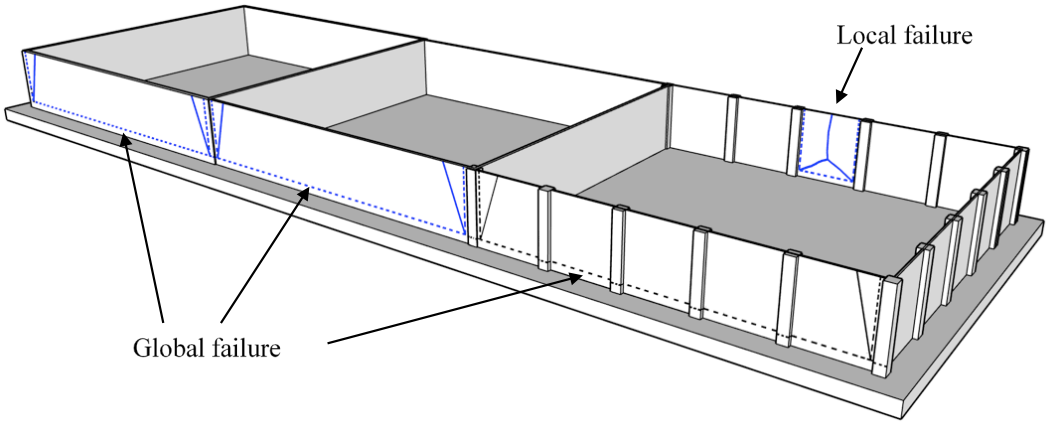

Figure 10. Illustration of local and global collapse mechanisms of the basins.

4.3. Computational Nonlinear Analysis

In order to validate the design assumptions and calculations highlighted above, a nonlinear analysis for representative "portions" of each of the three basins the pilot structure consists of was undertaken, also in view of the experimental validation currently ongoing, whose preliminary results are going to be shown hereafter. Details of the analyzed elements and representative, related positions in the pilot and cross sections are shown in Figure 11.

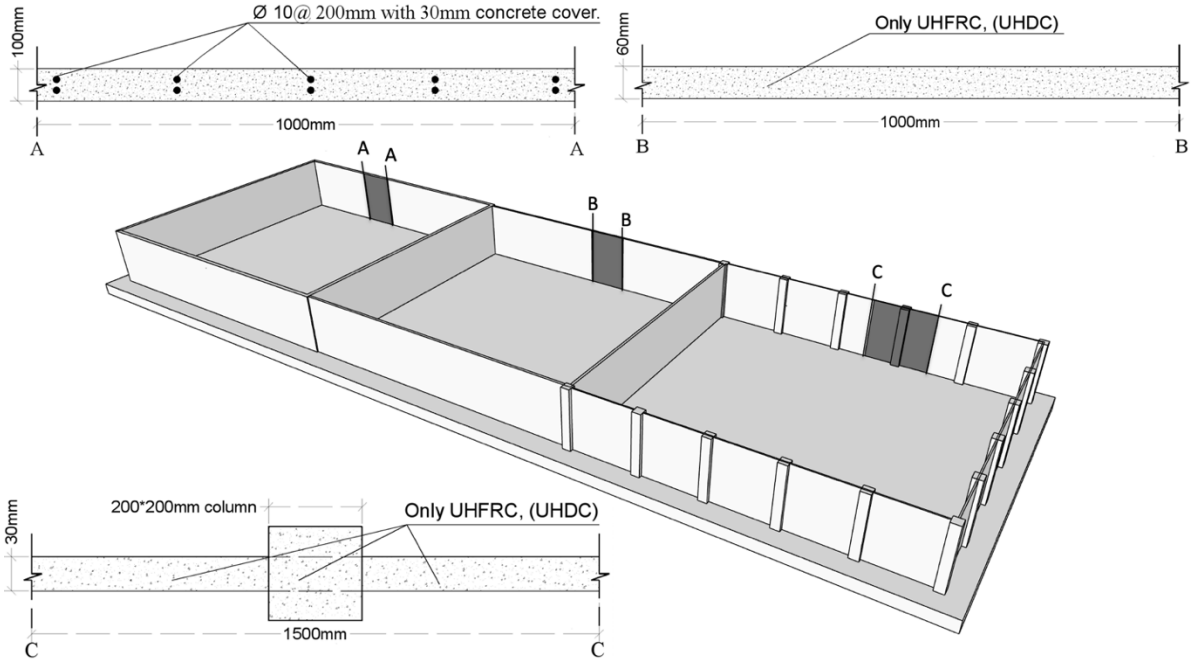

Figure 11. Sectional layout of the geothermal water basin walls assumed for nonlinear analysis.

4.3.1. Description of the Analysis Method

To perform the nonlinear analysis of each element, the fiber method was used, widely recognized as an efficient approach to perform the moment–curvature analysis of the reinforced concrete elements. Instead of evaluating the axial and flexural rigidity by finding the neutral axis corresponding to each strain increment, which is rather a time-consuming approach, the secant axial and flexural rigidity can be evaluated as $S_a = \frac{P}{\varepsilon_a}$, $S_b = \frac{M}{\phi}$, in order to calculate S_a and S_b corresponding to M and P.

The deformation vector $[\varepsilon_o \quad \emptyset]^t$ must be obtained first. A sectional tangent stiffness $[K_t]$ links an infinitesimal load vector $[dP \quad dM]^t$ and an infinitesimal deformation vector $[d\varepsilon \quad d\emptyset]^t$, as detailed in Equations (3) and (4).

$$dP = \frac{\partial P}{\partial \varepsilon} d\varepsilon + \frac{\partial P}{\partial \phi} d\phi \tag{3}$$

$$dM = \frac{\partial M}{\partial \varepsilon} d\varepsilon + \frac{\partial M}{\partial \phi} d\phi \tag{4}$$

$$\begin{bmatrix} dP \\ dM \end{bmatrix} = [K_t] \begin{bmatrix} d\varepsilon \\ d\emptyset \end{bmatrix} \tag{5}$$

Using this approach, and by dividing the concrete section into a sufficient number of fibers, strains in the middle of the strips can be iteratively imposed to find the solution. The Newton–Raphson method has been used to find the convergence of the solution with respect to the applied axial load. For a given axial strain and curvature, the strains in the middle of the strips and steel bars are evaluated as

$$\varepsilon_{strip} = \varepsilon_o + \phi * y_{strip}$$

$$\varepsilon_{steel} = \varepsilon_o + \phi * y_{steel}$$

Then, using the assumed concrete stress–strain constitutive laws, which will be specified hereafter for each of the investigated cases, stresses were evaluated at the center of each steel and concrete layers (strip) and, through suitable integration of the stresses over the concrete and steel fibers, the resultant axial force and bending moment were finally calculated.

4.3.2. Reinforced Ordinary Concrete Section (the First Basin)

The first basin was constructed using ordinary reinforced concrete, with a cross section as shown in Figure 12. Given the boundary condition and the applied load, the overall behavior of the wall is represented by a 1.5 m-long cantilever beam fixed at the base of the basin. The section shown in Figure 12 below has been analyzed for the moment–curvature relationship using the procedure described above. To proceed with the nonlinear sectional analysis, the material constitutive laws described in Figure 13 were implemented for concrete and steel bars, as described in the following section. The unconfined compressive stress–strain relationship described by Mander et al. [37] was adopted (Figure 13a), while the bilinear softening tensile stress–strain relationship shown in Figure 13b was used to describe the tensile behavior of the concrete [38]. Elastic–perfectly plastic steel behavior, shown in Figure 13c, is used to describe the constitute law of the steel bars.

A MATLAB-R2020a code was written for the computational nonlinear analysis. The code was programmed to stop and report the failure when the maximum compressive concrete strain in the extreme fiber reaches the ultimate compressive strain, $\varepsilon_{cu} = -3.5\%$.

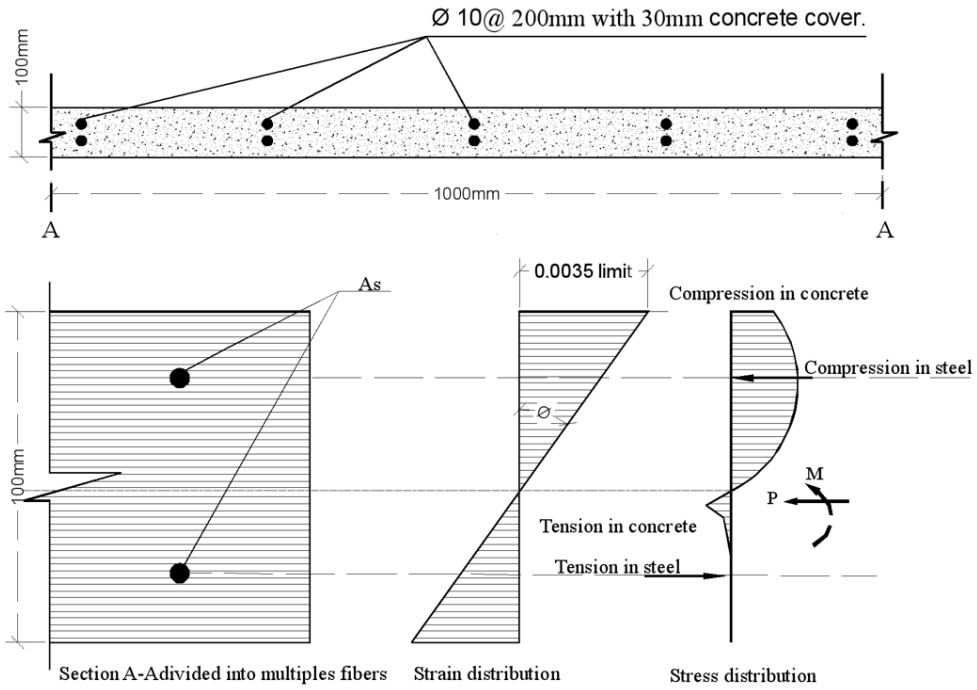

Figure 12. Ordinary reinforced concrete section analysis.

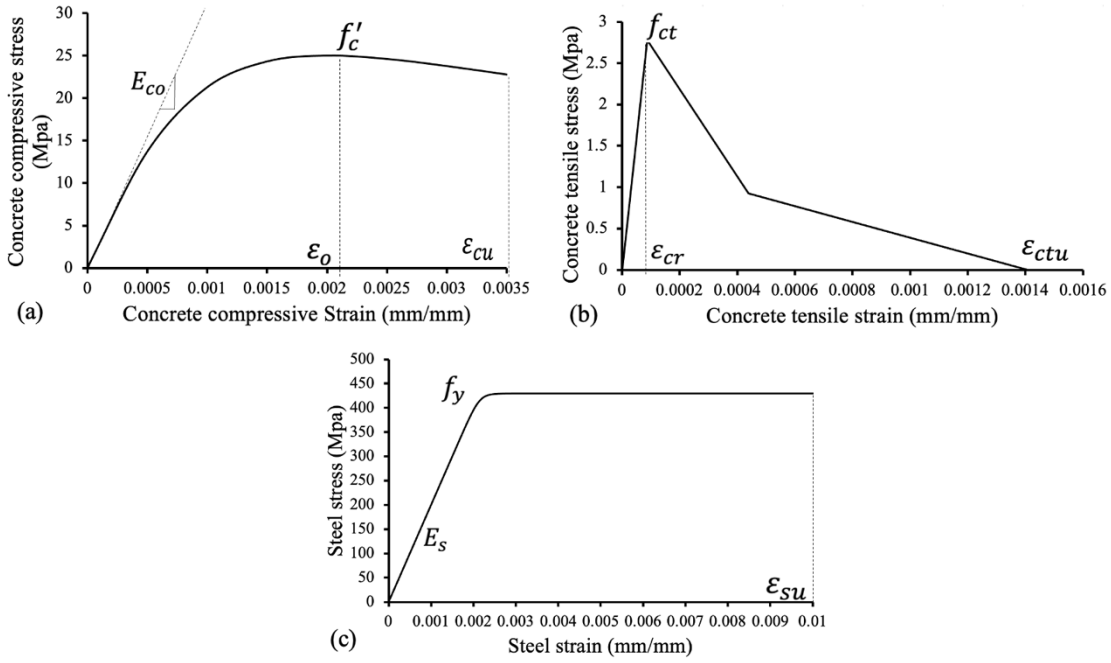

Figure 13. Materials constitutive relationships: (**a**) concrete compressive relationship, (**b**) concrete tensile relationship, and (**c**) steel compressive and tensile relationship.

4.3.3. UHDC Wall (Second Basin)

The same analysis procedure described previously was adapted for the second basin where the section consists of only UHPC material (Figure 14a). By implementing the concrete tensile stress–strain relationship adopted from Lo Monte and Ferrara (2020) [22], Figure 14b, the tensile behavior was identified. For the compressive stress–strain relationship, linear elastic behavior will be assumed with a modulus of elasticity of 41,700 MPa. The analysis of the section was programmed to terminate when the tensile strain at the extreme strip reaches the strain level of 0.015.

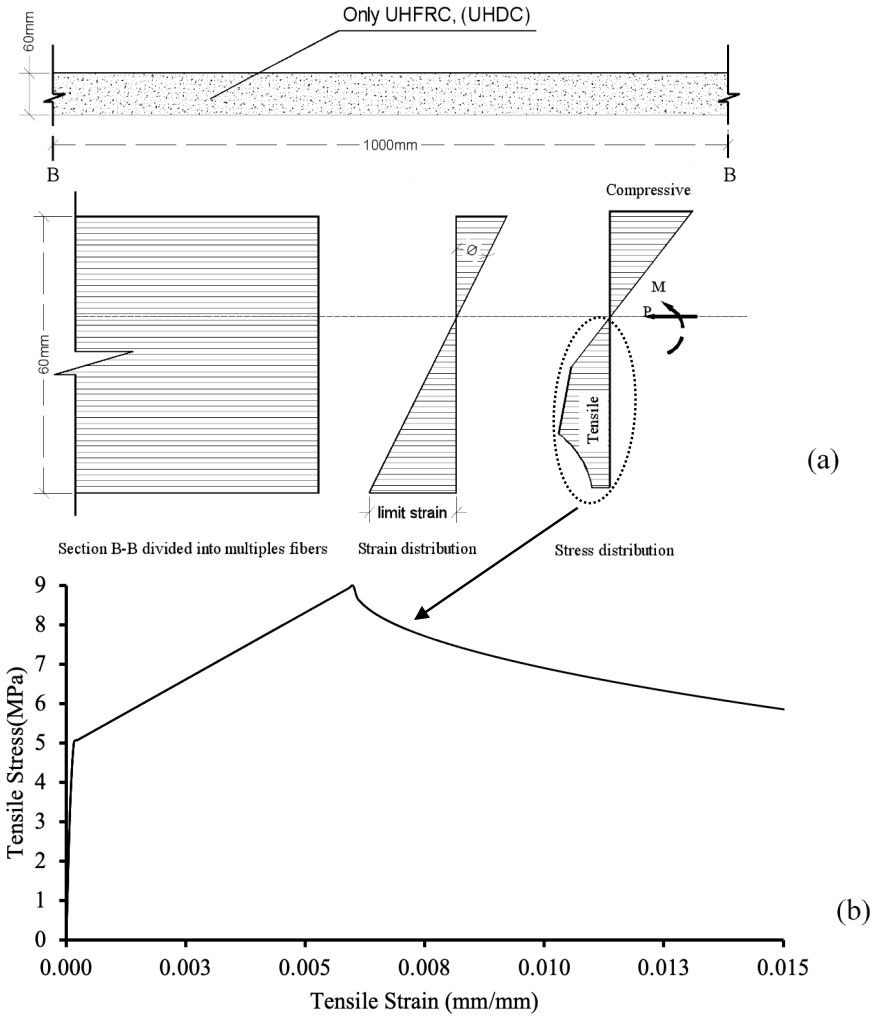

Figure 14. UHDC/UHPC sectional analysis by means of the fibers method (**a**), and the UHPC/UHDC tensile constitutive laws in term of strain (**b**).

4.3.4. UHDC Precast Slab Supported by UHDC Columns

The third cell of the basin is characterized by the 30 mm-thick precast UHPC/UHDC panels connected to each other through cast-in-place UHPC/UHDC columns where holes were made in the precast slabs along the vertical edges to increase the interlocking when the cast-in-place concrete of 200 × 200 mm^2 columns enters the holes and joins them together. For the connection of the system with the foundation, a groove was made in the foundation; then, the lower edge of precast elements, which also accommodates holes as the side edges, was inserted in the groove and the UHPC/UHDC concrete was poured into the groove to connect the foundation with the precast elements. However, the groove width was not sufficient to efficiently interlock with the lower part of the cast-in-place columns. Therefore, partial fixity or pin-end conditions were assumed during the analysis of the cross section, as shown in Figure 15, where, due to the applied load and expected behavior, the compression stress will be anticipated only in part of the column section and the precast slab has to equalize the compression force by performing in only tension behavior.

The results of the moment–curvature analysis results for all the sections are reported in Figure 16.

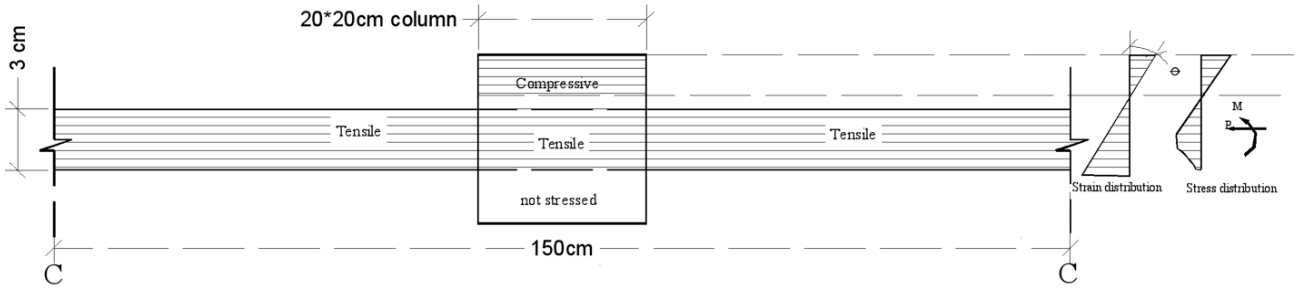

Figure 15. UHPC/UHDC precast panels supported by a UHPC/UHDC cast-in-place column.

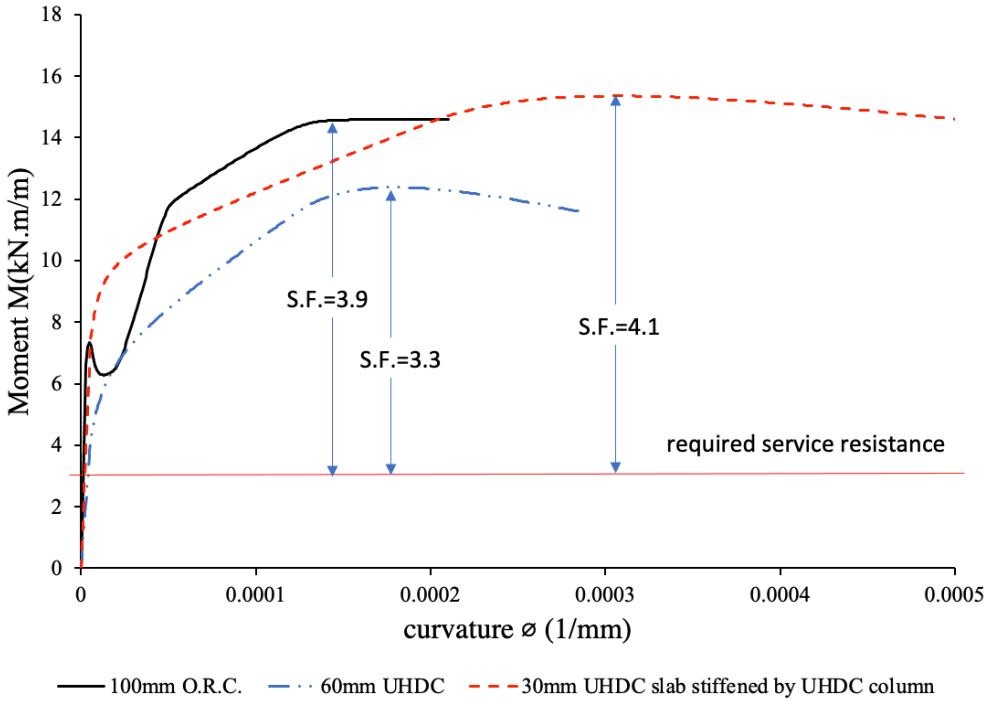

Figure 16. Moment–curvature relationship for the different employed sections.

4.4. Moment–Displacement Analysis

For the investigated structural elements, representative of the "current" development of the walls of the three basins, the maximum top edge deflection was also calculated by integrating the moment of area of the curvature diagram for each moment step, as shown in the formula below and illustrated in Figure 17.

$\Delta = \sum_{i=1}^{curvature\ points} \left(\frac{\emptyset_i * x_i + \emptyset_{i+1} * x_{i+1}}{2}\right) * dx(i)$ (sum of trapezoidal moment of area), where

x_i = distance from the position of xi to the wall's tip;

x_{i+1} = distance from the position of $xi + 1$ to the wall's tip;

$\emptyset_i$ = curvature corsponding to point x_i;

$\emptyset_{i+1}$ = curvature corsponding to point x_{i+1};

Δ = maximum displacement at the critical section.

A MATLAB code was employed to numerically integrate the curvature diagram for each step by creating loops to virtually create the span length and divided it into multiple segments (600–700 segments) based on the points of integration. Then, using the formula described above, the moment–displacement curves were obtained for each case. The moment–curvature graphs reported in Figure 16 were used to produce the moment–displacement graphs shown in Figure 18.

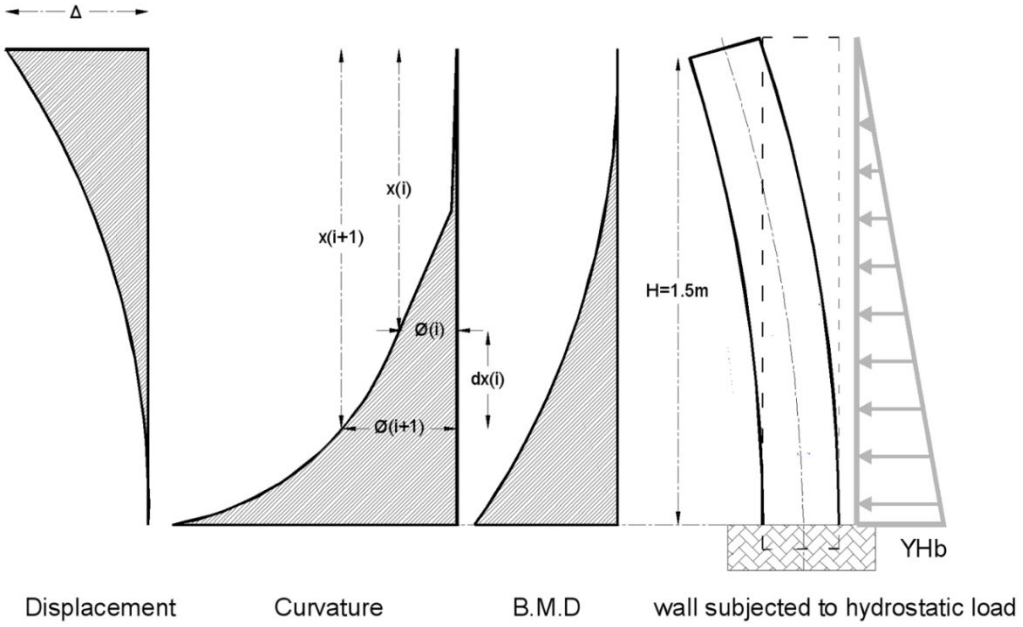

Figure 17. Illustration of displacement analysis using the moment of curvature area method.

Figure 18 compares the structural performance in terms of the water height–displacement/crack-width level for the three different structural element types (100 mm ordinary reinforced concrete wall, 60 mm cast in place UHDC wall and 30 mm precast UHDC panels joined by a 200 × 200 mm² cast-in-place UHDC wall). Moreover, the crack width, depth of compression zone and, where applicable, tensile strain of the longitudinal reinforcement bars are also reported for the three different sections.

Interestingly, it can be noticed that under a service water level around 130 cm, all the sections are not cracked, which satisfies the minimum requirements of the serviceability limit states for water-retaining walls for crack widths, and the maximum displacement at the tip point, which did not exceed 4 mm.

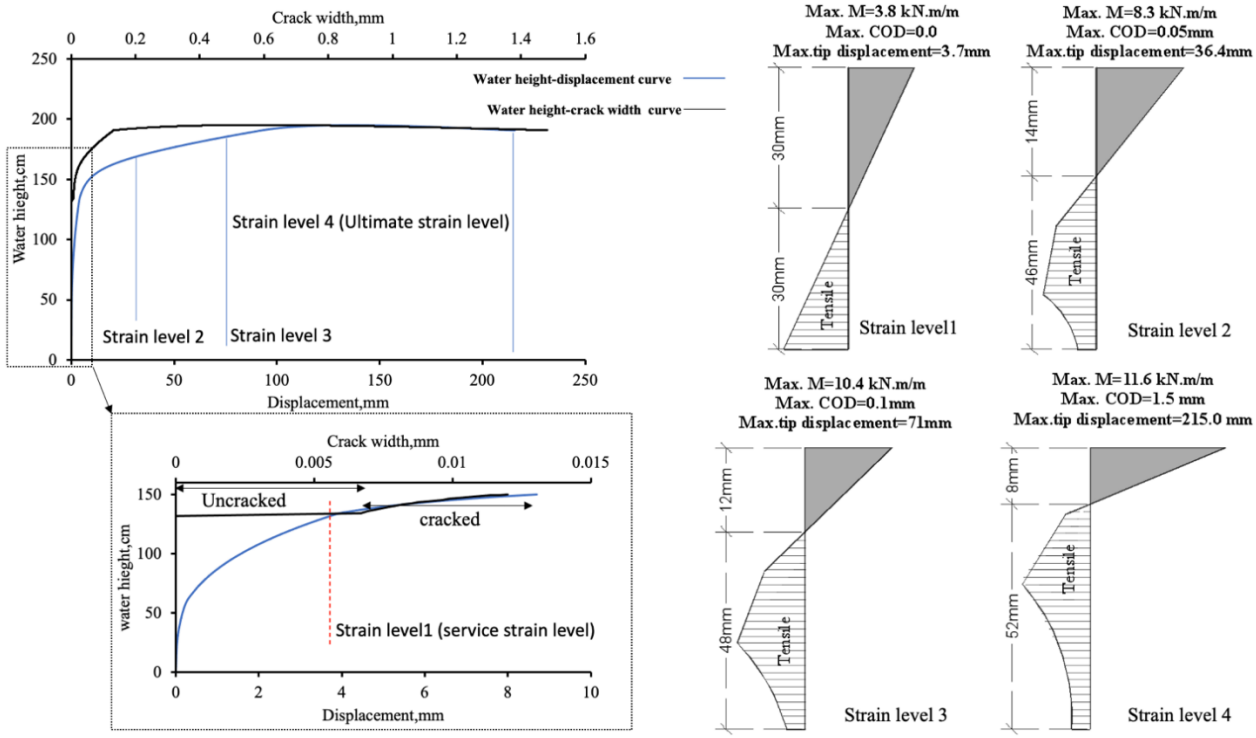

(**a**)

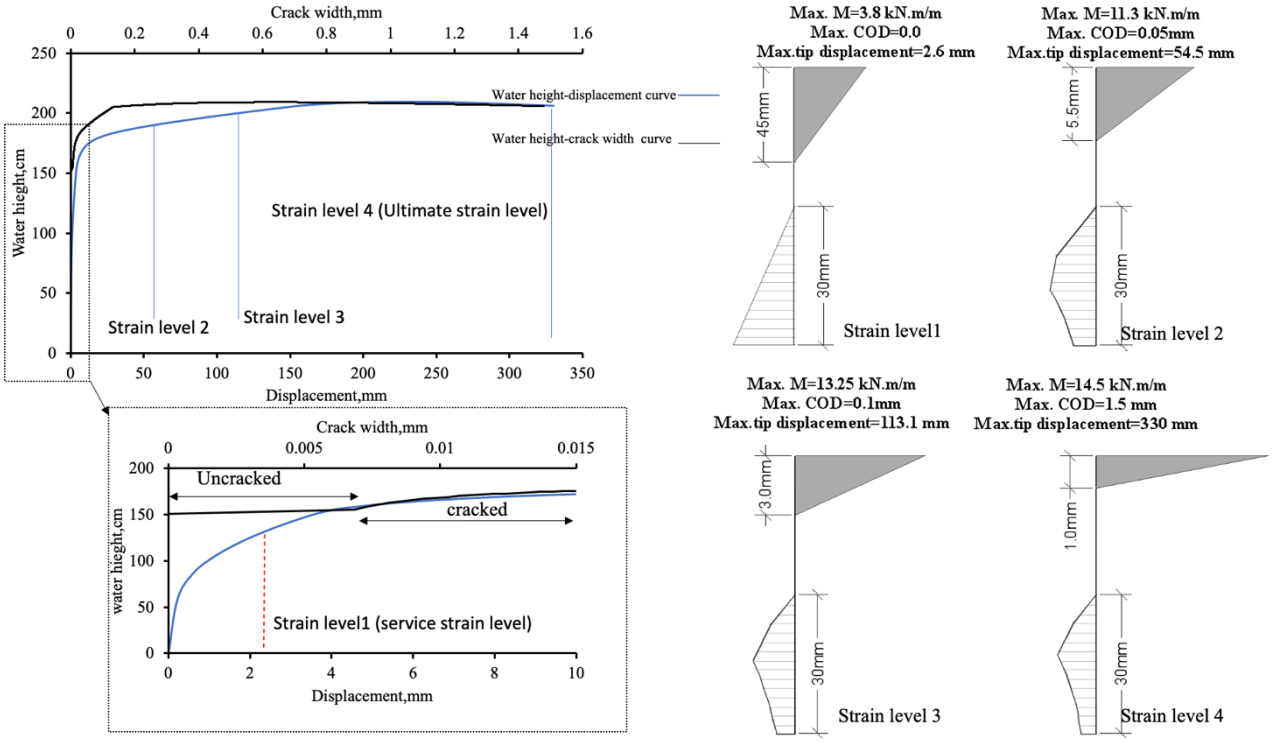

(**b**)

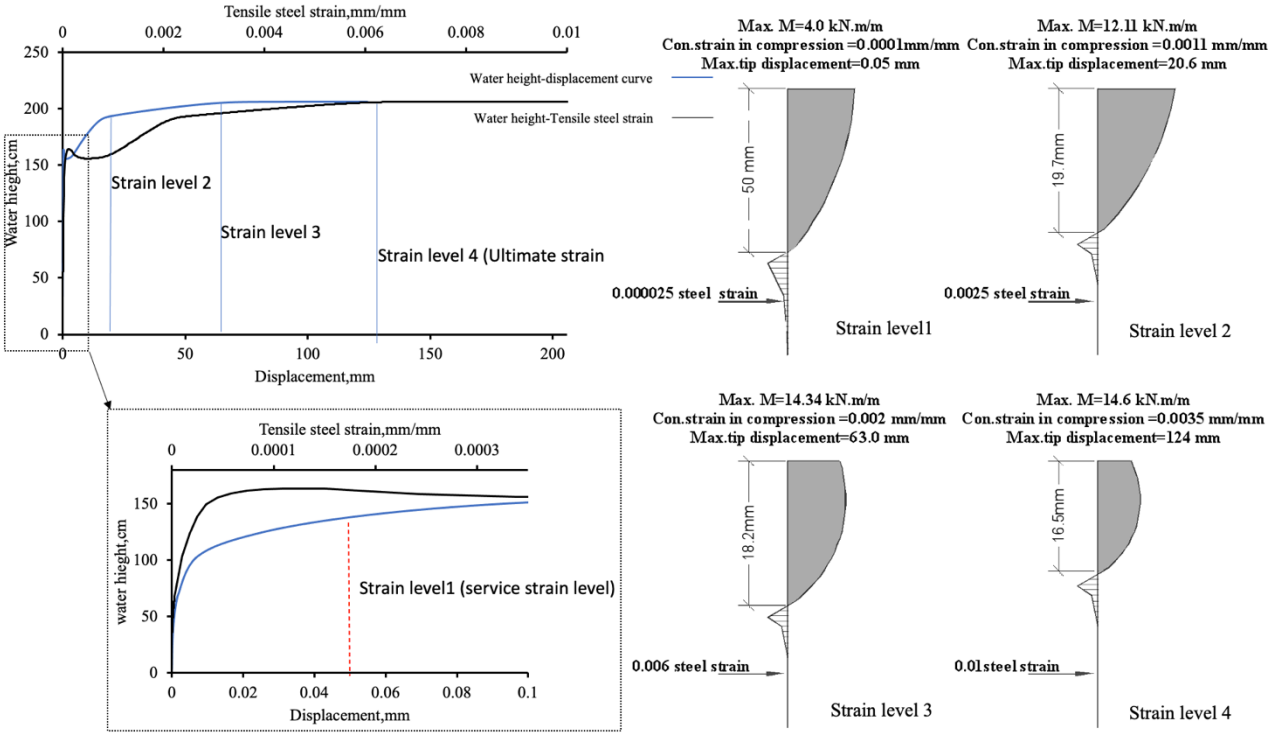

(**c**)

Figure 18. Sectional and structural analysis results for the three different structural element concepts: (**a**) 60 mm UHDC wall, (**b**) 30 mm UHDC slabs stiffened by a 20 × 20 cm² UHDC column, and (**c**) 100 mm ORC section wall.

Finally, looking into the ultimate limit states by gradually increasing the curvature and the strains of the tensile zone, the sections performed very well to resist a water level 1.5 times higher than the service water level even for the thin sections implemented with

UHDC materials, though this would correspond to an unrealistically high displacement of the top edge of the wall.

This interestingly confirms the importance of the Serviceability Limit State conditions as governing the design of structures made of Ultra-High-Performance Concrete, in this case also incorporating hybrid (ordinary steel + fibers) reinforcement and hence the need to develop and validate reliable design tools for the correct prediction of the structural behavior under the aforementioned conditions, including the cracked state, and for the crack width calculation.

5. Validation Tests on the Real Structure (EGP Pilot)

Within the framework of the ReSHEALience project, several validations of the six proof-of-concept pilot structures have been planned to investigate the durability and assess the reliability of the structural design concepts of the pilots designed and built using the formulated and tested UHDC materials. For the geothermal water basin structure built by the project partner Enel Green Power, the carried-out validation tests, performed in collaboration with the Politecnico di Milano team, consisted of non-destructive monitoring of concrete quality via a rebound hammer and Ultrasonic Pulse Velocity tests, steel fiber dispersion survey and water-height versus displacement monitoring during filling and emptying of the basins. These also included steel strain monitoring via strain gauges placed during the construction in Basin 1 (ordinary reinforced concrete structure), concrete strain monitoring via strain gauges placed on the upper surface of concrete elements and reinforcement corrosion potential assessment via sensors installed during the construction process.

5.1. Steel Fibre Dispersion Survey

Steel fiber dispersion was surveyed for specific precast and cast-in-place UHPC/UHDC elements, as illustrated in Figure 19 below. The magnetic method proposed and validated by Ferrara et al. [39] was adopted in this survey for its robustness and easiness to handle on the work site. The method uses a probe with sensors spaced at 160 mm, which create a magnetic field, sensitive to the magnetic properties of the steel fibers aligned within it, thus resulting in variation in the measured inductance when the sensor is leaned in contact to the surface of the basin wall, along a different specified direction. The results of the measurements were recorded via a MATLAB script. A detailed description of the method and its calibration can be found in [39–41].

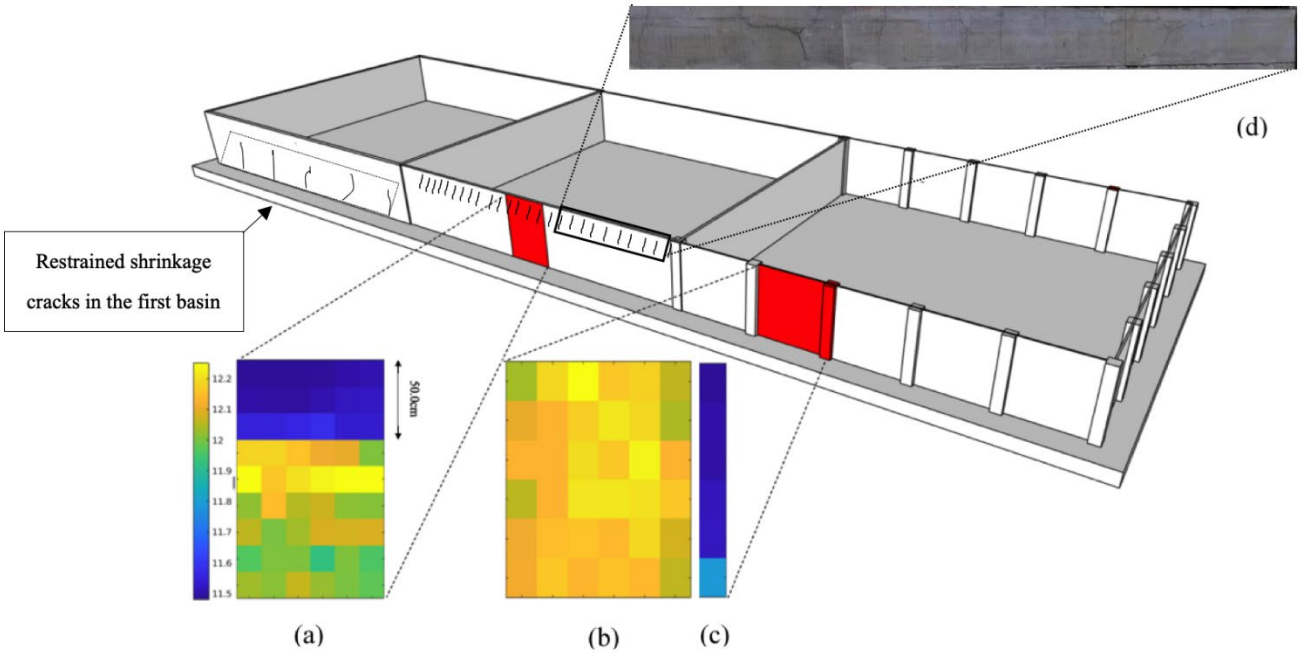

	ORC wall	UHDC wall
Estimated shrinkage wc (mm)	0.226	0.46
Measured wc (mm)	0.12	0.1
Healing index	46%	78%

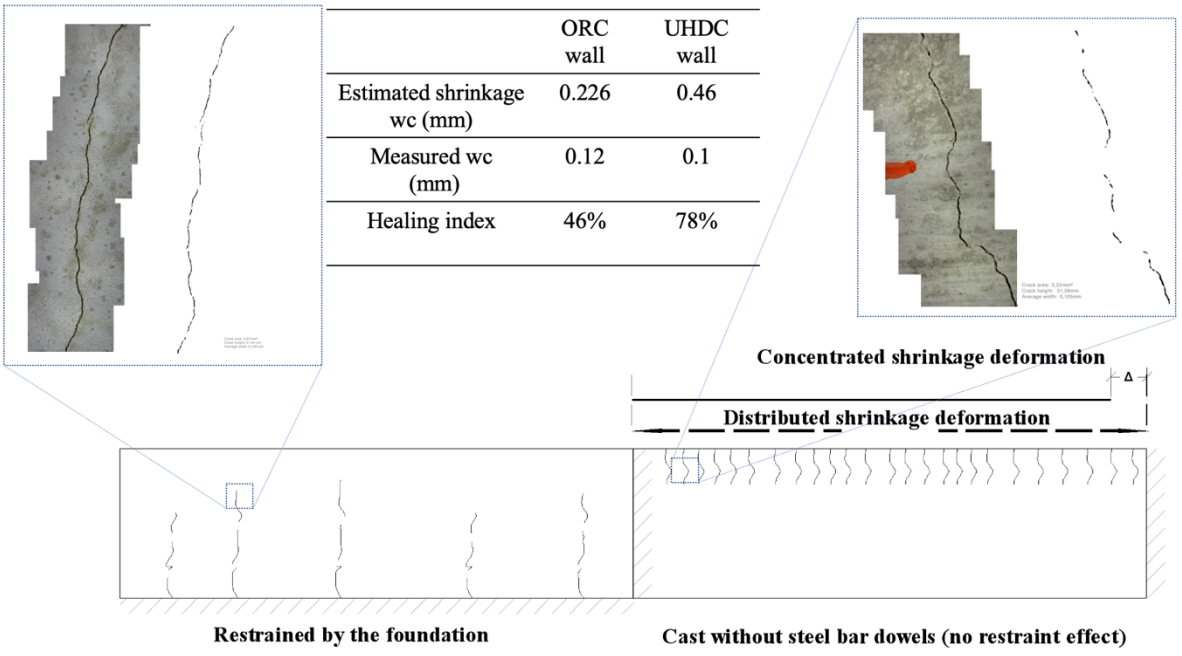

(**e**)

Figure 19. Steel fiber distribution for cast-in-place 6 cm wall (**a**), precast 3 cm slab (**b**), cast-in-place 20 × 20 cm column (**c**), shrinkage cracks distributed along the top portion of second basin (**d**), and the estimated versus measured shrinkage cracks for ORC (on left) and UHDC (on right) walls (**e**).

Results qualitatively plotted in Figure 19 indicate that fiber dispersion is quite homogenous for the pre-cast elements (b), which were casted horizontally. On the other hand, for the cast-in-place elements wall (a) and the column (c), some segregation of the steel fibers occurred in the top layers; this observation implies that the precast application of UHPC should be preferred, particularly for vertical structural elements where vertical casting may jeopardize the distribution of the steel fibers and affect the performance of the structural elements even prior to the application of the load.

This uneven distribution of the fibers resulted also into higher proneness to shrinkage cracking: as a matter of fact, equally spaced shrinkage cracks were observed in the top part of the 60 mm-thick wall. These cracks, spaced about 250 mm, extend about 500 mm downward from the top edge of the wall, which corresponds to the depth of the zone where a lack of steel fibers was detected through a non-destructive survey (Figure 19a). In fact, these cracks did not appear in the third basin where the wall is made with precast elements and the steel fibers were well distributed. Since these cracks are located at the top, they are believed to be due to the shrinkage deformation restrained by the constraints provided by the lateral walls located at the ends as well as by the bottom layers, richer in fibers; less effective crack control was found in this region poorer in fibers.

Figure 19e shows the simple model adopted by Destrée et al. [42] to estimate the crack width induced by shrinkage deformation in the UHDC wall, whereas the methodology illustrated in EN1992-1-1 [32] to estimate the restrained shrinkage crack width in basin one ORC wall for the UHDC section the steel fiber contribution was eliminated in the top part from the crack width calculation based on the steel fibers content survey. The calculated crack widths were compared to the measured ones after the basin have been exposed for more than a year, and a significant reduction in crack width is noticed, which could be attributed to the potential self-healing promoters or autogenous healing in UHDC and ORC walls, respectively. Evidence of crack sealing in the ORC and UHDC wall, as observed during a pilot testing on 14 May 2021, are shown in Figure 20.

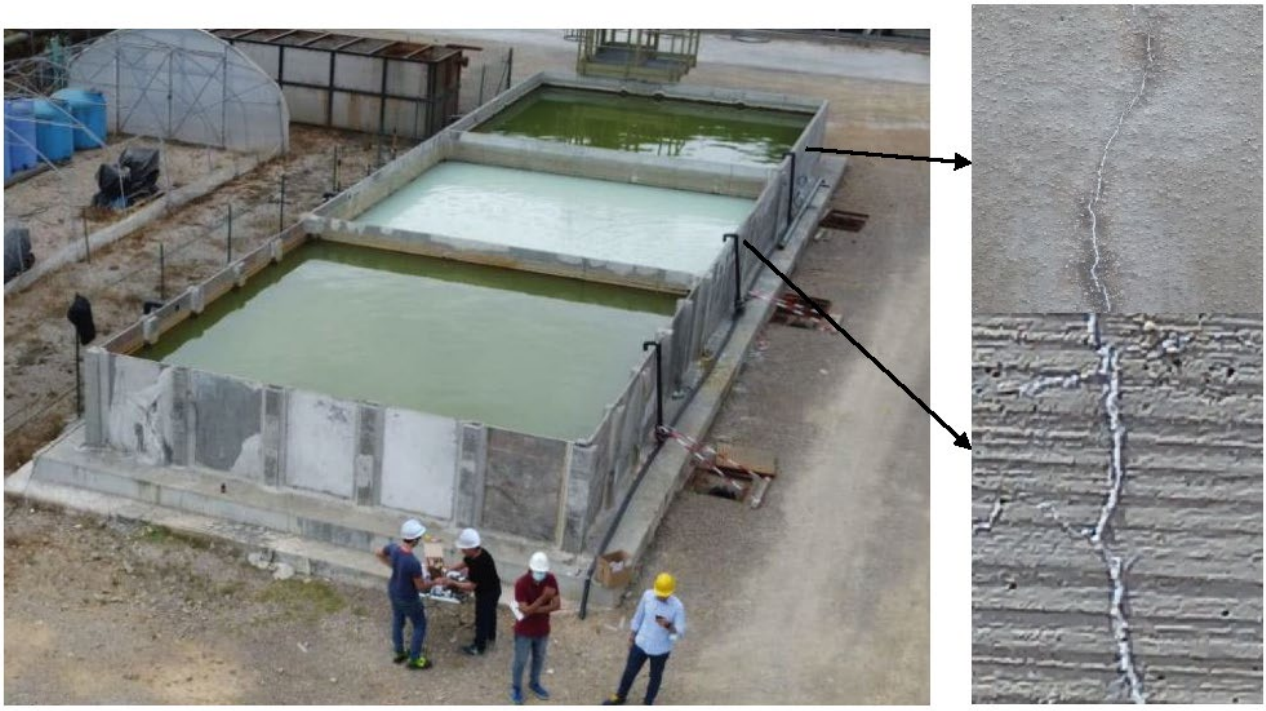

Figure 20. Evidence of crack sealing as monitored during a water filling test of the pilot on 14 May 2021.

5.2. Water Height–Displacement Relationship

In order to validate the assumption of the analysis for each section of the basin (30 mm UHPC/UHDC precast panels supported by a UHPC/UHDC cast-in-place column, 60 mm UHPC/UHDC wall and 100 mm reinforced concrete wall), the load or water height–displacement relationship was calculated for each section and compared to on-site measurements, where each cell of the basin was filled gradually and the displacement at the top and midpoint of the section was recorded, as shown in Figure 21. It can be also observed, where the numerical estimated water level height–displacement relationship is

compared to the experimental obtained one, that the two relationships are in a good agreement for the third basin, which validates the assumption of an inverted T-beam hypothesis in the third basin (precast UHDC slabs supported by UHDC columns). However, for the first, the numerical analysis exhibited a stiffer behavior, which could be attributed to the restrained shrinkage cracks that developed at the base of the wall, and reduces the stiffness of the section that is particularly responsible for the overall behavior of the wall. For the second basin, the 60 mm-thick UHDC wall, the experimental curve exhibits a stiffer response than the numerical one, which could be attributed to the additional stiffening contribution from the transverse action brought by the relatively thin section element.

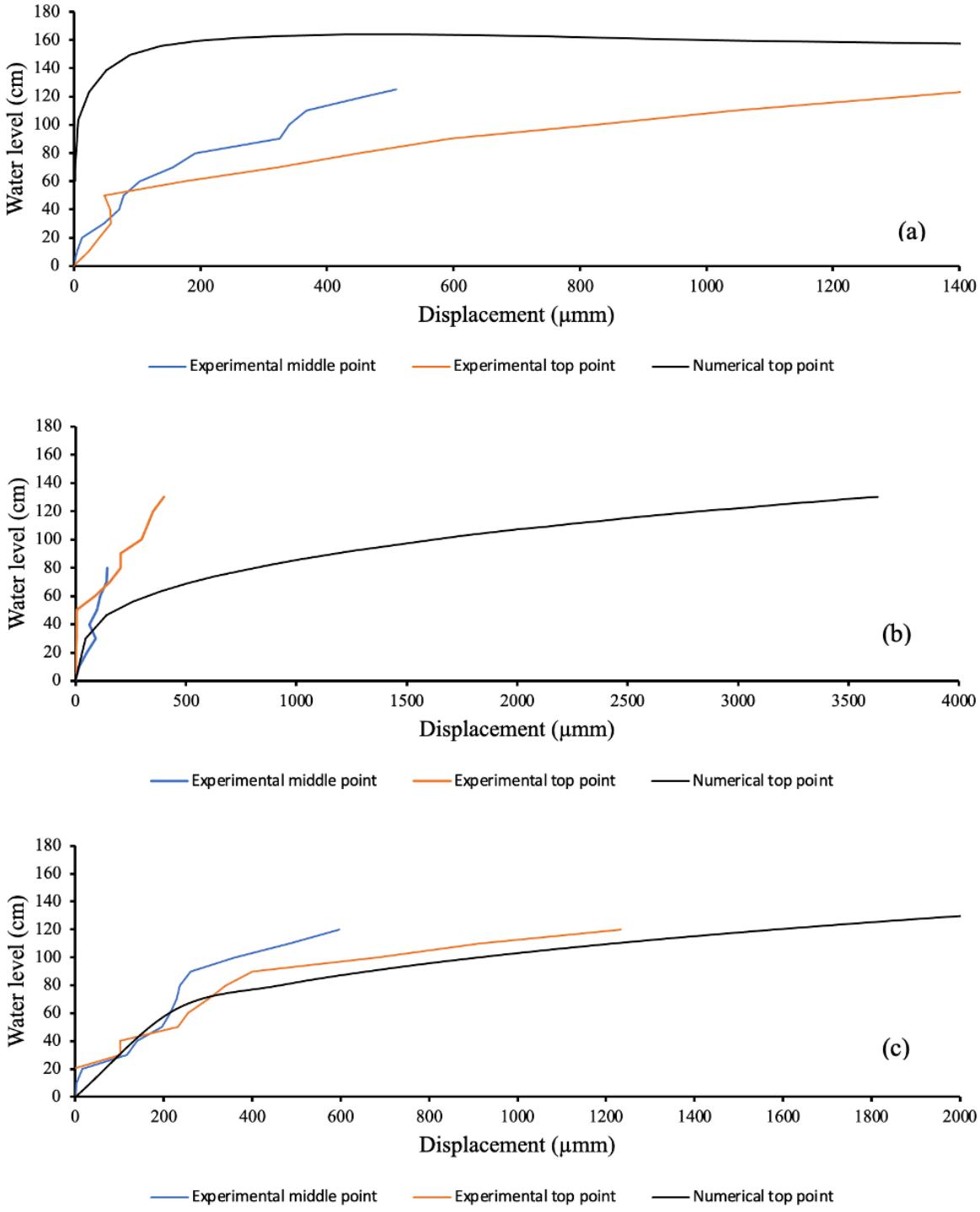

Figure 21. Water height versus displacement for the first (**a**), second (**b**) and third basin (**c**).

5.3. Crack Width and Water Tightness

As stated in the EN-1992—Part 3 [43], where liquid retaining and containment structures are addressed and reported in Table 6 below, the minimum thickness, minimum crack width and minimum depth of the compression zone were checked here for the basin. However, since the UHDC materials has the ability to control the crack width, accommodate residual tensile strain and healing/sealing of the up to 0.3 mm crack width under water immersion, this requirement is considered to be tolerable [44].

For instance, the requirements suggest a minimum thickness of the water retaining structure of 120 mm. This limited thickness is required to control the water tightness, However, for the UHDC walls Basin 2, which are 60 mm thick, and Basin 3, which are only 30 mm thick, the sectional nonlinear analysis indicates that these sections are not cracked under the service load level, despite some healable shrinkage cracks at the top of the second basin. According to Table 5, and depending on the leakage requirements, the tightness class is classified from 0 to 3. Class 1 tightness indicates that some amount of leakage is permitted, such as surface staining and damp patches. In this case, the requirement is limited the strain under service condition to 0.00015 mm/mm, which is exactly the same strain level calculated under service actions for Basin 2 walls and much higher than the tensile strain for the case of Basin 3 under the service load level. In fact, during the validation visits, some surface staining and damp patches occurred at the first time of filling but, interestingly, some of these cracks were completely sealed and some were partially healed, as observed and detailed in Figure 20 above.

The other aspect is the thickness of the compression zone depth for the sections of the walls under the service load level, as reported in Figure 18; the compression zone depths of all sections satisfies the water tightness requirements (20% of the section thickness).

Table 6. Prescriptions regarding liquid retaining and containment structures for the different tightness classes as per EN 1992—Part 3.

Class	Requirements for Leakage	Specific Requirements
0	Some degree of leakage acceptable, or leakage of liquids irrelevant.	Silos holding dry materials may generally be designed with this class.
1	Leakage to be limited to a small amount. Some surface staining or damp patches acceptable.	Any cracks expected to pass through the full thickness should be limited to $w_{k1,}$ Healing may be assumed if the expected range of strain under service condition is less than 150×10^{-6}.
2	Leakage to be minimal. Appearance not to be impaired by cracks.	Cracks should not pass through the full width of a section, the design value of the depth of the compression zone should be at least $x_{min.}$ x_{min} = min (50 mm or 0.2 h—h is the element thickness).
3	No leakage permitted.	

Further validation of these findings could pave the way for a suitable extension of the tightness class requirements for UHPC structures, considering material-specific mechanical and durability properties as well as typically employed construction technologies (e.g., pre-casting).

6. Final Discussion and Conclusions

The pilot concrete structure analyzed in this paper represents a tank to contain geothermal water in a geothermal power plant; the pilot has been constructed with different structural/sectional concepts according to the different employed materials (ordinary reinforced concrete and cast-in-situ/precast Ultra-High-Performance/Ultra-High-Durability Concrete). Giving the applied loads represented by the hydrostatic water pressure acting on the cantilever walls, and the mechanical properties of the materials as identified

through dedicated laboratory experimental campaigns, the structural systems were analyzed at both the ultimate and serviceability limit states in order to validate the design concepts. Upon entering the structure its service states (filled with 1.3 m of geothermal water), a series of full-scale field tests were also performed to validate the design's theoretical assumptions and the boundary conditions hypothesized, as also realized through the employed construction technologies. The most remarkable achievement is the reduction of the thickness from 100 mm in ordinary reinforced concrete to 60 mm in the case of UHDC cantilever walls and even less in the third basin (only 30 mm), where a solution based on precast slabs was implemented. The analysis at the ultimate limit state results in safety factors higher than 3 and 4 for the 60 mm-thick UHDC wall and 30 mm UHDC slabs supported by columns, respectively, as compared to 3.9 in the case of the 100 mm reinforced concrete section.

On the other hand, the serviceability analysis of the basin highlighted a very good performance in terms of crack-width limits and tightness, thanks to the mechanical performance of the UHDC materials. The serviceability analysis was also validated against the on-site observation and monitoring, where the filling and emptying of the basins were regularly carried out and no signs of leakages were observed.

Based on the evaluations presented in the paper, as corroborated by the on-site measurements as above, the following conclusions can be drawn:

- Among the employed UHDC structural solutions, the 30 mm-thick UHDC slabs supported by 200 × 200 mm UHDC columns performed better than the 60 mm UHDC cast-in-place wall in terms of steel fiber distribution, material consumption and structural performance under service and ultimate limit states.
- The nonlinear analysis carried out on Basin 2 and Basin 3 shows that the maximum expected crack width is very low, thanks to the signature tensile behavior of the employed UHPC/UHDC materials, to the benefit of the durability and overall long-term performance of the structure. The importance of the serviceability limit state conditions in governing the design of the structure is highlighted, as long as the superior mechanical and durability performance of the material (and the release of minimum cover/thickness constraints due to the complete elimination of conventional reinforcement replaced by dispersed fibers) do allow for a significant reduction in structural thickness.
- Load vs. displacements relationship as obtained by means of computational nonlinear analysis reasonably fit the corresponding curves obtained during the validation tests, confirming the reliability of the adopted construction processes and technologies and analysis methods.
- The site observation and monitoring proved the ability of the UHDC materials to heal and seal the small cracks after being filled with geothermal water, with a healing index close to 80%.
- The sections designed by using the UHDC materials exhibited very good serviceability performance although a significant reduction in the section thickness was used. The nonlinear analysis also allowed to confirm that the crack widths and compression zone thickness may fulfil the tightness class requirements, once suitable adaption to UHPC/UHDC materials can be made, exactly upon confirmation of the experimental and modelling findings herein highlighted.
- The numerical structural analysis results along with ultimate yield line mechanisms indicate that the second basin 60 mm UHDC section and the third section 30 mm UHDC section stiffened by 200 × 200 mm^2 UHDC columns can resist a hydrostatic pressure 1.5 times higher than the service load level before collapse.

Author Contributions: Preparation of the manuscript F.A., I.M., M.L. and S.S.; manage and supervision, F.L.M.; laboratory tests, P.B.; analysis of the yield line mechanisms, L.F.; defined the research concept, S.A.O. All authors have read and agreed to the published version of the manuscript.

Funding: The activity described in this paper has been performed in the framework of the project "Rethinking coastal defense and Green-energy Service infrastructures through enHancEd-durAbiLity high-performance cement-based materials-ReSHEALience", funded by the European Union Horizon 2020 research and innovation program under GA No 760824. The information and views set out in this publication are those of the authors and do not necessarily reflect the official opinion of the European Commission.

Institutional Review Board Statement: Not applicable.

Informed Consent Statement: Not applicable.

Data Availability Statement: this Data and further updates can be found here: [https://uhdc.eu/].

Conflicts of Interest: The authors declare no conflict of interest

References

1. Younis, A.; Ebead, U.; Suraneni, P.; Nanni, A. Cost effectiveness of reinforcement alternatives for a concrete water chlorination tank. *J. Build. Eng.* **2020**, *27*, 100992, doi:10.1016/j.jobe.2019.100992.
2. D3.2—Definition of key durability parameters for each scenario—ReSHEALience Available online: https://uhdc.eu/documentation/d3-2-definition-of-key-durability-parameters-for-each-scenario/ (accessed on 21 September 2020).
3. Thomas, M.; Bremner, T. Performance of lightweight aggregate concrete containing slag after 25 years in a harsh marine environment. *Cem. Concr. Res.* **2012**, *42*, 358–364, doi:10.1016/j.cemconres.2011.10.009.
4. Simultaneous Structural and Environmental Loading of an Ultra-High Performance Concrete Component|FHWA. Available online: https://highways.dot.gov/research/projects/simultaneous-structural-environmental-loading-ultra-high-performance-concrete-component (accessed on 13 June 2021).
5. Krelani, V.; Krelani, V.; Moretti, F. Autogenous healing on the recovery of mechanical performance of High Performance Fibre Reinforced Cementitious Composites (HPFRCCs): Part 2—Correlation between healing of mechanical performance and crack sealing. *Cem. Concr. Compos.* **2016**, *73*, 299–315, doi:10.1016/j.cemconcomp.2016.08.003.
6. Ferrara, L.; Krelani, V.; Moretti, F.; Roig Flores, M.; Serna Ros, P. Effects of autogenous healing on the recovery of mechanical performance of High Performance Fibre Reinforced Cementitious Composites (HPFRCCs): Part 1. *Cem. Concr. Compos.* **2017**, *83*, 76–100, doi:10.1016/j.cemconcomp.2017.07.010.
7. Cuenca, E.; Ferrara, L. Self-healing capacity of fiber reinforced cementitious composites. State of the art and perspectives. *KSCE J. Civ. Eng.* **2017**, *21*, 2777–2789, doi:10.1007/s12205-017-0939-5.
8. Yildirim, G.; Alyousif, A.; Şahmaran, M.; Lachemi, M. Assessing the self-healing capability of cementitious composites under increasing sustained loading. *Adv. Cem. Res.* **2015**, *27*, 581–592, doi:10.1680/adcr.14.00111.
9. Woyciechowski, P.P.; Kalinowski, M. The influence of dosing method and material characteristics of superabsorbent polymers (SAP) on the effectiveness of the concrete internal curing. *Materials* **2018**, *11*, 1600, doi:10.3390/ma11091600.
10. Wang, Y.S.; Alrefaei, Y.; Dai, J.G. Silico-aluminophosphate and alkali-aluminosilicate geopolymers: A comparative review. *Front. Mater.* **2019**, *6*, 106.
11. Ferrara, L.; Ozyurt, N.; Di Prisco, M. High mechanical performance of fibre reinforced cementitious composites: The role of "casting-flow induced" fibre orientation. *Materials and Structures* **2011**, *44*, 109–128.
12. Li, V.C.; Stang, H.; Krenchel, H. Micromechanics of crack bridging in fibre-reinforced concrete. *Mater. Struct.* **1993**, *26*, 486–494, doi:10.1007/BF02472808.
13. Al-Obaidi, S.; Bamonte, P.; Ferrara, L.; Luchini, M.; Mazzantini, I. Durability-based design of structures made with ultra-high-performance/ultra-high-durability concrete in extremely aggressive scenarios: Application to a geothermal water basin case study. *Infrastructures* **2020**, *5*, 1–44, doi:10.3390/infrastructures5110102.
14. Borg, R.P.; Cuenca, E.; Garofalo, R.; Schillani, F.; Nasner, M.L.; Ferrara, L. Performance Assessment of Ultra-High Durability Concrete Produced From Recycled Ultra-High Durability Concrete. *Front. Built Environ.* **2021**, *7*, 78, doi:10.3389/fbuil.2021.648220.
15. An Overview on H2020 Project "ReSHEALience"|Semantic Scholar. Available online: https://www.semanticscholar.org/paper/An-Overview-on-H2020-Project-"ReSHEALience"-Ferrara-Bamonte/9fc028915a762840ca6d11592b6acca013f4893b (accessed on 10 June 2021).
16. Alexander, M.G.; Ballim, Y.; Stanish, K. A framework for use of durability indexes in performance-based design and specifications for reinforced concrete structures. *Mater. Struct. Constr.* **2008**, *41*, 921–936, doi:10.1617/s11527-007-9295-0.
17. Alexander, M.G. Service life design and modelling of concrete structures—background, developments, and implementation. *Rev. ALCONPAT* **2018**, *8*, 224–245, doi:10.21041/ra.v8i3.325.
18. Simons, B. Concrete Performance Specifications: New Mexico Experience. *Concr. Int.* **2004**, *26*, 68–71.
19. Perspective on Prescriptions Available online: https://trid.trb.org/view/758581 (accessed on 13 June 2021).
20. Bickley, J.A.; Hooton, R.D.; Hover, K.C. Performance Specifications for Durable Concrete. *Concr. Int.* **2006**, *28*, 51–57.

21. Preparation of a Performance-based Specification for Cast-in-Place Concrete. Available online: https://www.yumpu.com/en/document/read/25802659/preparation-of-a-performance-based-specification-for-cast-in-place- (accessed on 13 June 2021).
22. Lo Monte, F.; Ferrara, L. Tensile behaviour identification in Ultra-High Performance Fibre Reinforced Cementitious Composites: Indirect tension tests and back analysis of flexural test results. *Mater. Struct. Constr.* **2020**, *53*, 1–12, doi:10.1617/s11527-020-01576-8.
23. Cuenca, E.; D'Ambrosio, L.; Lizunov, D.; Tretjakov, A.; Volobujeva, O.; Ferrara, L. Mechanical properties and self-healing capacity of Ultra High Performance Fibre Reinforced Concrete with alumina nano-fibres: Tailoring Ultra High Durability Concrete for aggressive exposure scenarios. *Cem. Concr. Compos.* **2021**, *118*, 103956, doi:10.1016/j.cemconcomp.2021.103956.
24. Cuenca, E.; Mezzena, A.; Ferrara, L. Synergy between crystalline admixtures and nano-constituents in enhancing autogenous healing capacity of cementitious composites under cracking and healing cycles in aggressive waters. *Constr. Build. Mater.* **2021**, *266*, 121447, doi:10.1016/j.conbuildmat.2020.121447.
25. Materazzi, A.L.; Ubertini, F.; D'Alessandro, A. Carbon nanotube cement-based transducers for dynamic sensing of strain. *Cem. Concr. Compos.* **2013**, *37*, 2–11, doi:10.1016/j.cemconcomp.2012.12.013.
26. Cuenca, E.; Rigamonti, S.; Gastaldo Brac, E.M.; Ferrara, L. Crystalline admixture as healing promoter in concrete exposed to chloride-rich environments: An experimental study. *ASCE J. Mater. Civ. Eng.* **2020**, in press, doi:10.1061/(ASCE)MT.1943-5533.0003604.
27. Li, V.C.; Leung, C.K.Y. Steady-State and Multiple Cracking of Short Random Fiber Composites. *J. Eng. Mech.* **1992**, *118*, 2246–2264, doi:10.1061/(asce)0733-9399(1992)118:11(2246).
28. Naaman, A.E.; Reinhardt, H.W. Proposed classification of HPFRC composites based on their tensile response. *Mater. Struct. Constr.* **2006**, *39*, 547–555, doi:10.1617/s11527-006-9103-2.
29. In Proceedings of the 2nd International Conference on UHPC Materials and Structures (UHPC2018-China), Fuzhou, China, 7–10 November 2018; Shi, C., Chen, B., Eds.; RILEM Pubs: Fuzhou, China, 2018; p. 832.
30. Li, V.C.; Mishra, D.K.; Wu, H.C. Matrix design for pseudo-strain-hardening fibre reinforced cementitious composites. *Mater. Struct.* **1995**, *28*, 586–595, doi:10.1007/BF02473191.
31. Upgrading the Concept of Uhpfrc for High Durability in the Cracked State: The Concept of Ultra High Durability Concrete (UHDC) in the Approach of the h2020 Project Reshealience—Core. Available online: https://core.ac.uk/display/195747484 (accessed on 13 June 2021).
32. *EN 1992-1-1: Eurocode 2: Design of concrete structures—Part 1-1: General rules and rules for buildings*; CEN: Brussels, Belgium, 2004.
33. NTC 2018: Norme tecniche per le costruzioni (Italian Guidelines for Constructions) Rome, Italy 2018; Volume 20.
34. Lo Monte, F.; Ferrara, L. Characterization of the Tensile Behaviour of Ultra-High Performance Fibre-Reinforced Concrete. In *Proceedings of the NBSC2019 Workshop*; IMReady; Milan, Italy, 2019; pp. 45–54.
35. Di Prisco, M.; Ferrara, L.; Lamperti, M.G.L. Double edge wedge splitting (DEWS): An indirect tension test to identify post-cracking behaviour of fibre reinforced cementitious composites. *Mater. Struct. Constr.* **2013**, *46*, 1893–1918, doi:10.1617/s11527-013-0028-2.
36. Timoshenko, S.P.; Woinowsky-Krieger, S. *Theory of Plates and Shells*; McGraw-Hill: New York, NY, USA, 1959.
37. Mander, J.B.; Priestley, M.J.N.; Park, R. Theoretical Stress-Strain Model for Confined Concrete. *J. Struct. Eng.* **1988**, *114*, 1804–1826.
38. Abdalla, H.M.; Karihaloo, B.L. A method for constructing the bilinear tension softening diagram of concrete corresponding to its true fracture energy. *Mag. Concr. Res.* **2004**, *56*, 597–604, doi:10.1680/macr.2004.56.10.597.
39. Ferrara, L.; Cremonesi, M.; Faifer, M.; Toscani, S.; Sorelli, L.; Baril, M.A.; Réthoré, J.; Baby, F.; Toutlemonde, F.; Bernardi, S. Structural elements made with highly flowable UHPFRC: Correlating computational fluid dynamics (CFD) predictions and non-destructive survey of fiber dispersion with failure modes. *Eng. Struct.* **2017**, *133*, 151–171, doi:10.1016/j.engstruct.2016.12.026.
40. Ferrara, L.; Faifer, M.; Toscani, S. A magnetic method for non destructive monitoring of fiber dispersion and orientation in steel fiber reinforced cementitious composites-part 1: Method calibration. *Mater. Struct. Constr.* **2012**, *45*, 575–589, doi:10.1617/s11527-011-9793-y.
41. Ferrara, L.; Faifer, M.; Muhaxheri, M.; Toscani, S. A magnetic method for non destructive monitoring of fiber dispersion and orientation in steel fiber reinforced cementitious composites. Part 2: Correlation to tensile fracture toughness. *Mater. Struct. Constr.* **2012**, *45*, 591–598, doi:10.1617/s11527-011-9794-x.
42. Destrée, X.; Yao, Y.; Mobasher, B. Sequential Cracking and Their Openings in Steel-Fiber-Reinforced Joint-Free Concrete Slabs. *J. Mater. Civ. Eng.* **2016**, *28*, 04015158, doi:10.1061/(asce)mt.1943-5533.0001377.
43. EN 1992-1-1. *Eurocode 2-Design of Concrete Structures-Part 3: Liquid Retaining and Containment Structures*; CEN: Brussels, Belgium, 1992; Volume 4.
44. Cuenca, E.; Tejedor, A.; Ferrara, L. A methodology to assess crack-sealing effectiveness of crystalline admixtures under repeated cracking-healing cycles. *Constr. Build. Mater.* **2018**, *179*, 619–632, doi:10.1016/j.conbuildmat.2018.05.261.